JGR Oceans

RESEARCH ARTICLE
10.1029/2022JC019012

Key Points:

- Paleo-proxy based reconstructions of hourly coastal water level components are produced using a stochastic water level emulator
- Considering natural variability in water levels over 1500–2000 CE increases coastal flood risk beyond that suggested by instrumental records
- When superimposed on sea-level rise, natural variability in coastal water level can significantly increase extreme coastal water levels

Supporting Information:

Supporting Information may be found in the online version of this article.

Correspondence to:

S. Mukhopadhyay,
sm2798@cornell.edu

Citation:

Mukhopadhyay, S., Leung, M., Cagigal, L., Kucharski, J., Ruggiero, P., & Steinschneider, S. (2023). Understanding the natural variability of still water levels in the San Francisco Bay over the past 500 yr: Implications for future coastal flood risk. *Journal of Geophysical Research: Oceans*, *128*, e2022JC019012. https://doi.org/10.1029/2022JC019012

Received 23 JUN 2022
Accepted 23 JAN 2023
Corrected 16 FEB 2023 and 24 FEB 2023

This article was corrected on 16 FEB 2023 and 24 FEB 2023. See the end of the full text for details.

Author Contributions:

Conceptualization: Sudarshana Mukhopadhyay, John Kucharski, Peter Ruggiero, Scott Steinschneider
Formal analysis: Sudarshana Mukhopadhyay, Meredith Leung
Funding acquisition: John Kucharski, Peter Ruggiero, Scott Steinschneider
Investigation: Sudarshana Mukhopadhyay, Meredith Leung
Methodology: Sudarshana Mukhopadhyay, Meredith Leung, Laura Cagigal, Peter Ruggiero, Scott Steinschneider

Understanding the Natural Variability of Still Water Levels in the San Francisco Bay Over the Past 500 yr: Implications for Future Coastal Flood Risk

Sudarshana Mukhopadhyay[1], Meredith Leung[2], Laura Cagigal[3], John Kucharski[4], Peter Ruggiero[2], and Scott Steinschneider[1]

[1]Department of Biological and Environmental Engineering, Cornell University, Ithaca, NY, USA, [2]College of Earth, Ocean, and Atmospheric Sciences, Oregon State University, Corvallis, OR, USA, [3]Department of Sciences and Technologies of Water and Environment, Universidad de Cantabria, Santander, Spain, [4]Institute for Water Resources, Hydrologic Engineering Center, Davis, CA, USA

Abstract Increasing exposure to coastal flood hazards will potentially induce an enormous socio-economic toll on vulnerable communities. To accurately characterize the hazard, we must consider both natural water level variability and climate change-induced sea-level rise. In this study, we develop a paleo-proxy-based reconstruction of coastal flood events over the last 500 yr to capture natural water level variability and superimpose that reconstruction onto expected sea-level rise to explore interannual and multidecadal variability in plausible future coastal flood risk. We first develop reconstructions of leading principal components (PCs) of sea surface temperature anomalies from 1500 CE onwards, using tree-ring, coral, and sclerosponge chronology-based El Niño Southern Oscillation reconstructions as predictors in a wavelet autoregression model. These reconstructions of PCs are then used in a stochastic water level emulator to develop ensemble simulations of hourly still water levels (SWLs) in the San Francisco Bay. The emulator accounts for multiple relevant processes, including monthly mean sea level (MMSL) anomalies, storm surge, and tide, all varying at different timescales. Accounting for natural variability in water levels over 1500–2000 CE increases coastal flood risk beyond that suggested by instrumental records alone. When superimposed on 0.22 m of sea-level rise (approximately the amount experienced over the previous century), the simulations show that while high tides and large storm surges cause the smaller extreme SWLs, the larger extreme SWLs occur during concurrent high MMSL, high tides, and significant storm surges. Our findings thus highlight the need to consider natural water level variability for coastal adaptation and planning.

Plain Language Summary Increasing exposure to coastal flood hazards will potentially induce an enormous socio-economic toll on vulnerable communities. To accurately characterize the flood risk, we must consider both natural water level variability and climate change-induced sea-level rise. But we need long records of sea level conditions to quantify the natural variability and characterize the associated extreme flood levels. Paleo-proxies, such as corals, sponges, and tree rings, capture these long-term conditions during times when modern instrumental records were unavailable. Using this paleo-proxy-based data, we have developed 500 yr long simulations of coastal water levels using specialized computer models that account for several climate and weather patterns and estimates of sea surface temperature conditions from 1500 to 2000. We use these long simulations to quantify the natural fluctuations in coastal water levels at annual and decadal time scales. When we consider the full extent of such fluctuations, coastal flood risk increases beyond the current flooding thresholds in San Francisco Bay, our study site. Our findings suggest a strong need to account for natural water level fluctuations in addition to projections of sea-level rise for any future coastal adaptation planning.

1. Introduction

It is well established that coastal flooding will increase with projected sea level rise (SLR; Sweet & Park, 2014; Thomson et al., 2021; Trenberth et al., 2015). Even a modest amount of SLR can result in disproportionately large (Kriebel et al., 2015; Vitousek et al., 2017) or exponential (Taherkhani et al., 2020) increases in coastal flood frequency, causing larger floods that threaten infrastructure and vulnerable communities (Moftakhari et al., 2015, 2017; Neumann et al., 2015). However, the extent of future coastal flooding does not depend solely

Project Administration: John Kucharski, Peter Ruggiero, Scott Steinschneider
Software: Sudarshana Mukhopadhyay, Meredith Leung, Laura Cagigal
Validation: Sudarshana Mukhopadhyay, Meredith Leung
Visualization: Sudarshana Mukhopadhyay, Meredith Leung
Writing – original draft: Sudarshana Mukhopadhyay, John Kucharski, Peter Ruggiero, Scott Steinschneider
Writing – review & editing: Sudarshana Mukhopadhyay, Peter Ruggiero, Scott Steinschneider

on climate change induced SLR but also on natural variability in water levels, defined here as temporal fluctuations in water levels not attributable to systematic long-term SLR trends. This study advances methods used to quantify natural variability in coastal water levels, which is a key step in describing future coastal flooding hazards.

Coastal flooding depends on variability in total water levels (TWLs) resulting from processes that vary over a range of spatiotemporal scales (Anderson et al., 2019; Barnard et al., 2019; Leonard et al., 2014). These include (a) regional relative SLR, (b) storm surge, (c) wave setup and swash, (d) high-frequency (i.e., diurnal cycles, Haigh et al., 2020), and low-frequency (4.4 yr perigean and 18.6 yr nodal cycles; Peng et al., 2019; Rashid et al., 2021; Thompson et al., 2021) fluctuations in astronomical tides, and (v) non-tidal variations in mean sea level (MSL) due to seasonal, interannual, and decadal fluctuations in atmospheric and oceanographic forcing (Anderson et al., 2019; Barnard et al., 2019; Calafat et al., 2013; Dangendorf et al., 2014; Hermans et al., 2020; Merrifield et al., 2012; Orton et al., 2016; Ray & Foster, 2016; Sweet & Park, 2014; Taherkhani et al., 2020; Thomson et al., 2021; Vitousek et al., 2017; Wahl & Chambers, 2016). These processes can either dampen or amplify TWLs based on the synchronization of their phases. Therefore, the joint variability and dynamics of water level components must be understood to characterize coastal flooding hazards (Anderson et al., 2019; Barnard et al., 2019; Nederhoff et al., 2021; Parker et al., 2019; Serafin et al., 2017; Thompson et al., 2021), particularly when they are combined with projected SLR scenarios (Hinkel et al., 2021; Wahl et al., 2017).

Most state-of-the-art coastal flood hazard studies model variability in TWLs and extreme sea levels (ESLs) using a combination of statistical (Anderson et al., 2019; Rueda et al., 2016) and hydrodynamical (Barnard et al., 2019, 2014) modeling approaches. Statistical methods such as extreme value analysis are used to estimate the distribution of ESLs from tide gauge records (Ghanbari et al., 2019; Ray & Foster, 2016; Thomson et al., 2021). The choice of frequency distribution in extreme value analysis can impart significant biases in ESL estimation (Hinkel et al., 2021; Wahl et al., 2017), although non-stationary approaches (Haigh et al., 2010) usually mitigate some of this bias (Mentaschi et al., 2016; Wahl & Chambers, 2015). If not accounted for, statistical dependence between components of ESLs, such as storm surge, wave runup, tidal, and fluvial processes, can also lead to significant bias in ESL assessments (Arns et al., 2020), as can the limited length of observations in the instrumental record (Moftakhari et al., 2015; Wahl et al., 2017).

To overcome these limitations, a variety of methods have been forwarded to produce very long-time series of TWLs that account for interactions between meteorological, oceanographic, and hydrological drivers that may or may not have occurred in the instrumental record. One approach employs hindcasts from coupled climate and ocean system models (Lang et al., 2019; Muis et al., 2016; Vitousek et al., 2017), though these simulations can be very computationally expensive. Other approaches employ statistical methods including Monte Carlo simulations (Serafin & Ruggiero, 2014) and joint probability models (Callaghan et al., 2008). Hybrid methods are also available. For instance, Haigh et al. (2014) used stochastically simulated storm records to drive a hydrodynamical model and assess coastal vulnerability to cyclonic storm surge events in Australia. Anderson et al. (2019, 2021) developed the Time-varying Emulator of Short and Long-term Analysis (TESLA) for coastal flood hazard assessment and applied the approach in San Diego, CA, by linking emulated TWLs with synoptic scale climate patterns at interannual (El Niño Southern Oscillation, ENSO) through intra-seasonal (Madden Julian Oscillation, MJO) timescales. Importantly, few statistical emulators (Anderson et al., 2019; Cagigal et al., 2020, 2021) incorporate atmospheric forcing, which can be crucial for understanding the drivers of extreme coastal flood events as suggested by Barnard et al. (2015) and Marcos et al. (2015).

Extreme value analysis techniques can be applied to synthetic sea level time series to better understand coastal flood variability and hazard potential. Using these techniques, global assessments of modeled storm surges (Muis et al., 2016) and amplification of flood frequency with projected SLR (Vitousek et al., 2017) have revealed important modes of variability in coastal flooding driven by different processes. However, even synthetic time series are sometimes too short to reveal important patterns of variability if they are limited to the ~40 yr of data available in modern reanalysis products. This point was highlighted in Lang et al. (2019), which used simulated sea levels for the German Bight over the past 1,000 yr from an Earth systems model to show that multidecadal to centennial variability in extreme flood events are difficult to capture using conventional approaches, and that long-term ensemble simulations of sea level are an important tool for quantifying flood risk.

These types of large ensemble simulations are particularly critical for decomposing low-frequency variability in coastal water levels and ESLs across various process drivers. Such decompositions have grown in popularity

over the last decade but have mostly been limited to shorter observational records. For instance, ESL variability at interannual to decadal scales has been linked to variability in climate forcing using statistical (Frederikse et al., 2016; Marcos et al., 2015; Wahl & Chambers, 2015, 2016), theory-based (Calafat et al., 2013), and ocean system (Thompson & Mitchum, 2014) models based on tide-gauge records. Similarly, Rashid et al. (2019) used a non-stationary generalized extreme values (GEV) distribution (Coles, 2001) derived from tide-gauge records across the coastal United States to develop ESL indicators that measure interannual to decadal variability in MSL and storm surge. Incorporating low-frequency variability in ESLs can significantly improve coastal flood risk assessments and help communities prepare for higher economic losses (Rashid et al., 2021). However, the lack of long-term tide-gauge records and very long ensemble simulations of coastal water levels limits our understanding of low-frequency natural variability in ESLs, and how this variability interacts with variability at higher frequencies to determine the full range of plausible sea levels that define coastal flood hazards.

In this study, we explore multi-timescale natural variability in coastal flooding through innovative uses of the paleorecord to reconstruct plausible sequences of water levels and the likelihood of coastal flood events. Past studies have used a combination of tree rings and marine and nearshore paleo proxies, including geochemical proxies, to reconstruct total seasonal precipitation (Chen et al., 2015; Neukom et al., 2014; Williams et al., 2021), extreme precipitation (Borkotoky et al., 2021; Steinschneider et al., 2016, 2018), regional moisture transport (Mukhopadhyay et al., 2018; Zheng et al., 2021), drought (Baek et al., 2019; McCabe et al., 2008; Woodhouse et al., 2010), global surface temperature (Osman et al., 2021), terrestrial climate (Krapp et al., 2021), SSTs (Emile-Geay et al., 2013, 2015; Freund et al., 2019), and sea surface salinity (Nurhati et al., 2011). These studies rely on robust relationships between environmental signals embedded within networks of paleo-proxies and large-scale oceanic and atmospheric conditions that determine the likelihood of those environmental responses. Those same oceanic and atmospheric conditions can influence the likelihood of MSL anomalies and storminess patterns that influence storm surge, suggesting that similar reconstructions can be used to better understand past variability in coastal water levels and potentially pre-historic flood frequency. While regional numerical studies (Lang et al., 2019) have used paleo data-informed reanalysis of ocean systems models, to our knowledge paleo proxy data has not yet been utilized directly in statistical and hydrodynamic coastal flood models.

Building on the work in Anderson et al. (2019), which used monthly sea surface temperature anomalies (SSTAs) in the equatorial Pacific Ocean to drive stochastic simulations of coastal water levels (1880–2000 CE), this paper uses tree-ring, coral, and sclerosponge-based ENSO reconstructions to simulate past variability in SSTAs and water levels over the last 500 yr (1500–2000 CE). We focus on understanding natural variability in still water levels (SWLs; i.e., a composite of all tidal and non-tidal components of TWL except wave driven and river delivered water levels) in San Francisco Bay, California. The simulations are analyzed to evaluate natural variability in SWL and its components at interannual and-decadal timescales. The following research questions are addressed: (a) Can paleo-proxy based ENSO reconstructions be used to simulate long-time series of past SWLs? (b) How much coastal flood risk can be explained by natural variability, especially low-frequency variability of non-tidal processes? (c) How has coastal flood risk evolved in the San Francisco Bay over the past 500 yr, and what does this imply about future coastal flood risk? (d) What is the fractional contribution of SWL components to large flooding events?

2. Data

2.1. Input Data for SWL Emulator

We analyze the natural variability of coastal flood risk in the San Francisco Bay using TESLA, a statistical emulator of coastal water levels presented in Anderson et al. (2019). Past studies have successfully applied the TESLA framework at other tide gauge locations such as San Diego (Anderson et al., 2019, 2021), Oregon (Leung et al., 2019) as well as different islands in the Pacific region (Marra et al., 2022). Following that study, we use several different atmospheric and oceanographic data sets for developing synthetic SWL time series, which we summarize here (see Anderson et al., 2019 for more detail). Average monthly SSTAs over the equatorial Pacific Ocean (120°E–180°E, 5°N–5°S, at 2.5° resolution) are calculated from the Extended Reconstructed Sea Surface Temperature v4 data set (ERSSTv4; Huang et al., 2015) for the period 1880–2018 by removing 11 yr running averages for each month. The monthly SSTA values at each longitude are averaged to construct Hovmöller diagrams (Hovmöller, 1949) that capture SSTA variability from June to the following May by preserving monthly spatio-temporal behavior of SSTAs. Principal component (PC) analysis in Hovmöller space reveals three leading

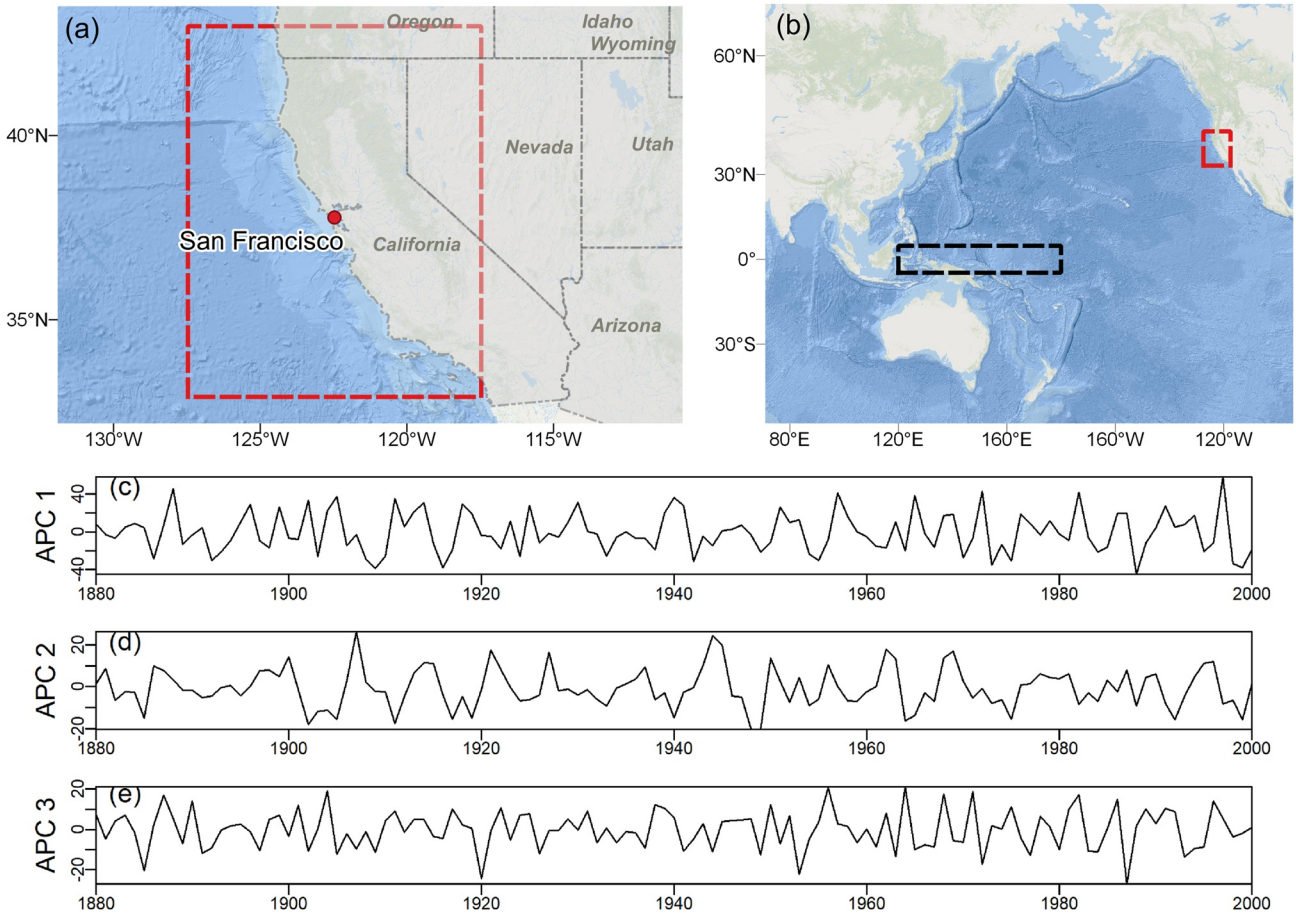

Figure 1. (a) Location of San Francisco tide gauge. (b) Regions bounded by the black dashed lines denote the spatial coverage of the equatorial Pacific region over which sea surface temperature anomalies (SSTAs) are calculated using ERSSTv4 data set. Regions bounded by the red dashed lines denote the spatial coverage of the 10° × 10° bounding box over which principal components of the local sea level pressure predictor are calculated. (c–e) Historical time series of annual principal components (APCs) of SSTAs in Hovmöller space.

EOFs defined at an annual timescale that explain 48%, 11%, and 7% of the variance, respectively (see Figure 1). The first PC (hereafter referred to as annual PC_1 in Hovmöller space, or APC_1) represents canonical interannual ENSO variability. APC_1 has high correlations with the average annual Oceanic Niño Index ($R^2 = 0.94$) and average annual Niño 3.4 index ($R^2 = 0.91$). APC_2 is associated with transient seasonal anomalies in the eastern Pacific region, while APC_3 exhibits a spatio-temporal pattern comparable to an eastward propagating Kelvin wave during boreal summer and fall. These three APCs in Hovmöller space, defined over 121 yr (1880–2000), are our initial target variables for reconstruction and are ultimately used to drive stochastic simulations of SWLs in TESLA.

In addition to the APCs, TESLA uses two leading PCs of daily outgoing long-wave radiation related to the MJO and its longitudinal phases from 1975 onwards (Wheeler & Hendon, 2004), which are taken from the Australian Bureau of Meteorology. The two leading MJO PCs are subsequently clustered into eight longitudinal phases and three categories of convection strength (Lafleur et al., 2015). Furthermore, TESLA uses sea level pressure (SLP) and squared SLP gradients from the National Centers for Environmental Prediction Climate Forecast System Reanalysis (CFSR, Saha et al., 2011) that cover the wave generation area relevant to San Francisco as defined by ESTELA (Pérez et al., 2014). Daily PCs of SLP and SLP gradients are clustered using a *k*-means algorithm into 36 weather types representing synoptic daily weather. These same SLP fields are also averaged to a monthly scale in a 10° × 10° bounding box (at 0.5° resolution) around the San Francisco Bay, and monthly PCs are calculated. We select 36 weather types to ensure that there are at least 60 days under each weather type in the historical record. Past studies (Anderson et al., 2019; Cagigal et al., 2020; de Souza et al., 2022) have identified 36 weather types to be adequately representative of synoptic daily weather conditions, excluding tropical cyclones. For calculating monthly PCs using monthly averages of SLP fields, we select the 10° × 10° bounding box after a

Table 1
Details of El Niño Southern Oscillation (ENSO) Reconstructions Explored to Develop Sea-Surface Temperature Anomaly Reconstructions

Data source/study	Variable	Spatial coverage of reconstruction	Temporal coverage (CE) of reconstruction	Paleo proxy data
Freund et al. (2019)	**Seasonal SST anomaly for NCT and NWP**	**5°S–5°N, 170°W–120°E**	**1617–2008**	**Network of 27 corals and sclerosponges**
Li et al. (2013)	**Niño 3.4 index**	**5°S–5°N, 170°W–120°E**	**1301–2005**	**2222 tree-ring chronologies**
Cook et al. (2008)	Niño 3.4 index	5°S–5°N, 160°W–150°E	1300–1979	404 Tree-ring chronologies from Mexico and Texas
Tierney et al. (2015)	SST	10°N–10°S, 85°E–175°W	1607–1997	57 tropical coral data sets
Emile-Geay et al. (2013)	Niño 3.4 index	5°S–5°N, 162.5°W–120°E	1150–1995	Annually resolved globally distributed 36 proxy records of corals, tree-ring records, marine sediment core, ice cores.
Sanchez et al. (2020)	Niño 3.4 index	5.8°N–3.9°S, 159.28°E–162.13°W	1863–2016	Oxygen isotopes from corals and sclerosponges
Datwyler et al. (2019)	First principal component of ENSO	5°N–5°S, 170°–120°W	1000–2014	Multiproxy (81 globally distributed proxy records including ice core, tree ring, corals, lake sediments etc.)
Wilson et al. (2010)	Niño 3.4 index	5°S–5°N, 170°W–120°E	1540–2007	Corals, tree-ring, and ice cores
Nurhati et al. (2011)	SST	5.87°N–5.87°S, 162.13°E–162.13°W	1886–1998	Corals and sclerosponges

Note. The ENSO reconstructions ultimately selected to support annual principal component reconstruction are highlighted in bold.

rigorous sensitivity analysis (Table S1) in which we study the influence of bounding box size and resolution on the predictive skill of the derived monthly PCs for the prediction of MMSL.

Observed SWLs in the San Francisco Bay are obtained from the National Oceanic and Atmospheric Administration (NOAA) tide gauge 9414290 (see Figure 1). The time series of storm surge is extracted using the hourly tide gauge record following a frequency domain decomposition after removing MSL and monthly to seasonal sea level anomaly components (Serafin & Ruggiero, 2014).

2.2. ENSO Reconstruction Data

We consider previously developed ENSO reconstructions to help reconstruct the APCs described in Section 2.1 above. These ENSO reconstructions are based on combinations of annually or seasonally resolved tree-rings, corals, sclerosponges, marine sediment cores, and ice core records (Table 1). The ENSO reconstruction that stretches back furthest begins in 1000 CE (Datwyler et al., 2019), while the reconstruction that begins latest ranges from 1886 to 1998 (Nurhati et al., 2011). Most of these reconstructions target the Nino 3.4 index (Cook et al., 2008; Emile-Geay et al., 2013; Li et al., 2013; Sanchez et al., 2020; Wilson et al., 2010), but others target other aspects of equatorial Pacific SSTAs. For instance, Freund et al. (2019) use a network of 27 corals and sclerosponges to reconstruct seasonal anomalies in the Niño Cold Tongue (NCT) in the Eastern Pacific and Niño Warm Pool in the Central Pacific, thereby resolving differences between Eastern El Niño and Central El Niño events.

3. Methods

We first present an overview of TESLA, the time varying emulator for short and long-term analysis of coastal flooding, presented in Anderson et al. (2019) (Section 3.1). The emulator relies in part on equatorial Pacific SSTAs (the APCs described above in Section 2.1), which we reconstruct using paleo proxy-based ENSO reconstructions (Section 3.2). Specifically, we use a coupled linear regression and Wavelet Auto-Regression Model (WARM; Kwon et al., 2007) to simulate leading APCs back to 1500 CE. TESLA then uses the reconstructed APCs to generate ensembles of synthetic hourly SWL time series from 1500 to 2000 CE. These time series are used to make inferences about extreme SWL variability over last 500 yr (Sections 3.3 and 3.4). Figure 2 provides a schematic representation of this workflow.

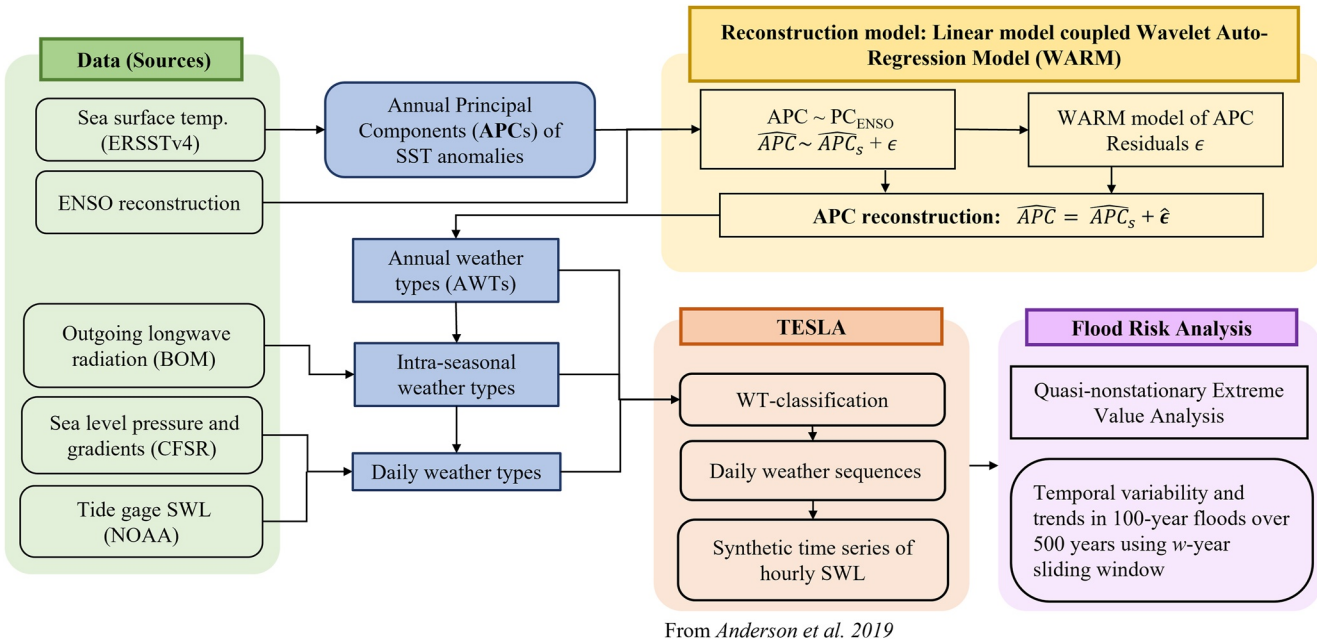

Figure 2. Schematic diagram of overall workflow with Time-varying Emulator of Short and Long-term Analysis (TESLA) module adapted from Anderson et al. (2019). The Sea surface temperature (ERSSTv4) anomalies are used to compute the annual principal components (APCs) first. APCs and El Niño Southern Oscillation (ENSO) reconstructions are used to develop APC reconstruction using the linear model coupled Wavelet Auto-regression model (yellow box). APC reconstructions inform the Annual weather types. The data inputs (green boxes) for Intra-seasonal and daily weather types (bottom two blue boxes) inform the TESLA framework (orange box), which is used to generate synthetic time series of hourly still water level (SWL) from 1500 to 2000 CE. Lastly, a flood risk analysis is carried out (violet box) using the SWL and its components to understand the temporal variability of flood risk and the effect of natural variability and sea level rise.

3.1. SWL Emulation With TESLA

SWL reconstructions are developed using the TESLA model (Anderson et al., 2019), which we briefly describe here. At any location, TESLA represents TWLs as a linear superposition of processes, driven by oceanographic, hydrologic, and meteorological forcings:

$$\mathrm{TWL} = \mathrm{SWL} + R \tag{1a}$$

$$\mathrm{SWL} = \eta_{\mathrm{MSL}} + \eta_A + \eta_{\mathrm{SE}} + \eta_{\mathrm{MMSLA}} + \eta_{\mathrm{SS}} \tag{1b}$$

Here, η_{MSL} is the MSL, η_A is the astronomical tide, and nontidal components $\eta_{\mathrm{SE}}, \eta_{\mathrm{MMSLA}}$, and η_{SS} are seasonal water level anomalies, monthly mean sea level anomalies (MMSLA), and variability due to storm surge, respectively. R denotes wave runup, including wave setup and swash, which can dominate TWLs on outer coast beaches (e.g., Serafin et al., 2017). At the tide gauge location within the enclosed San Francisco Bay, wave runup can be assumed negligible.

TESLA uses Pacific SSTAs (i.e., the APCs in Hovmöller space) in two stages to model SWL variability: (a) to simulate weather types, which, at a daily scale, connect synoptic weather to local conditions that drive high-frequency components of SWL (η_{SS}); and (b) to explain monthly to seasonal scale variability ($\eta_{\mathrm{SE}} + \eta_{\mathrm{MMSLA}}$) in SWLs. In the first stage, TESLA employs the APCs in a statistical downscaling approach that links climate patterns (or weather types) at different time scales to synoptic daily weather patterns, which in turn regulate variability in SWLs. Specifically, weather types at annual, intra-seasonal, and daily scales represent variability in ENSO, MJO, and SLP, respectively. Simulation of SWLs follows the following hierarchical process: (a) annual weather types (AWTs) are selected from a k-means clustering based on the three leading APCs. (b) Intra-seasonal weather types are developed by clustering the two leading PCs of outgoing longwave radiation to represent categorical MJO states. (c) An autoregressive logistic regression model then simulates synthetic daily weather types conditioned on weather types at annual, intra-seasonal, and antecedent daily time scales. (d) Finally, synthetic time series of storm surge at an hourly time scale are generated using joint probability distributions (Gaussian copulas) of sea state parameters defined separately for different daily weather types. Those joint probability distributions were fit using storm surge observations.

In the second stage, TESLA models slowly evolving monthly to seasonal components of SWLs (hereafter called $\eta_{\mathrm{MMSL}} = \eta_{\mathrm{SE}} + \eta_{\mathrm{MMSLA}}$) using a multivariate regression model parameterized with the three APCs and three local SLP-derived monthly scale PCs (MPCs, see Section 2.1) as covariates. The regression is comprised of the six covariates along with representations of the 12-month (annual) cycle:

$$\begin{aligned}\eta_{\mathrm{MMSL}} = \eta_{\mathrm{SE}} + \eta_{\mathrm{MMSLA}} = \\ = a_0 + a_1\mathrm{APC}_1 + a_2\mathrm{APC}_2 + a_3\mathrm{APC}_3 + a_4\mathrm{MPC}_1 + a_5\mathrm{MPC}_2 \\ + a_6\mathrm{MPC}_3 \\ + (b_0 + b_1\mathrm{APC}_1 + b_2\mathrm{APC}_2 + b_3\mathrm{APC}_3 + b_4\mathrm{MPC}_1 + b_5\mathrm{MPC}_2 \\ + b_6\mathrm{MPC}_3)\cos(2\pi t) \\ + (c_0 + c_1\mathrm{APC}_1 + c_2\mathrm{APC}_2 + c_3\mathrm{APC}_3 + c_4\mathrm{MPC}_1 + c_5\mathrm{MPC}_2 \\ + c_6\mathrm{MPC}_3)\sin(2\pi t)\end{aligned} \tag{2}$$

This model is fit to observed values of η_{MMSL} at a specific tide gauge location over the historical period. We remove a linear SLR trend and adjust the local MSL datum from the raw tide gauge data before calculating observed values of η_{SE} and η_{MMSLA}. In Equation 2, t represents the fractional year (day in year/total days in year) and η_{MMSL} is modeled at a monthly resolution. Annual scale harmonics are included using the periodic functions of $\sin(2\pi\omega t)$ and $\cos(2\pi\omega t)$ with $\omega = 1$ to capture seasonal variability. The regression model ultimately explains approximately 65% of the observed variance in MMSL (see Figure S1a in Supporting Information S1).

To account for the tidal component of SWL (η_A in Equation 1), a deterministic astronomical tide time series is added to the non-tidal SWL components. We simulate this tide time series using UTide (Codiga, 2011) at present-day MSL (η_{MSL}). Thus, the MSL and tidal components are together accounted for in this time series and are hereafter referred to as η_{Tide}. Finally, we add back the observed linear SLR trend of 0.0022 m/yr starting from 1900 to get a total of 0.22 m SLR over the most recent century in the simulation period (1900–2000). The SLR trend is derived from the observed tide gauge time series at San Francisco Bay (Figure S1b in Supporting Information S1).

3.2. SSTA and SWL Simulations Using ENSO Reconstructions

Interannual to decadal variations in the leading three APCs of SSTAs in Hovmöller space guide TESLA simulations. We utilize previously developed ENSO reconstructions (Table 1) to reconstruct these APCs for the past 500 yr, which are then input into TESLA to generate hourly reconstructions of η_{MMSL} and η_{SS} over the same time period, as described in Section 3.1.

For each APC_i ($i = 1, 2, 3$), we first select the ENSO products from Table 1 that lead to the best reconstruction. An initial screening process based on stepwise regression suggests that only one ENSO reconstruction product should be selected for each APC (see Supporting Information, Figures S2–S4 in Supporting Information S1). Therefore, for APC_i we select the single best ENSO reconstruction (ENSO_i) to use in a linear regression fit to data between years t = 1,880, …,2,000:

$$\mathrm{APC}_{t,i} = \beta_{0,i} + \beta_i\mathrm{ENSO}_i + \epsilon_{t,i}\ i = 1, 2, 3 \tag{3}$$

To assess model fit, we use a five-fold leave-25 yr out cross-validation, in which five combinations of consecutive 25 yr of data are withheld from the full data set of 121 yr, and the model is fit to the remaining 96 (or 97) yr of remaining data. We then estimate the APCs for the withheld 25 yr and repeat this process to generate out-of-sample APC estimates for the entire 121 yr data set. For each APC regression model, performance is measured using the cross-validated R^2 between historical APCs and out-of-sample predictions (Figure S5 in Supporting Information S1). For those ENSO reconstruction products that do not extend to 2000, we shorten the length of each of the five folds to accommodate the overlapping period between the ENSO product and the APCs.

As with all regression models, predictions from the regressions in Equation 3 represent the conditional expectations of each APC given values for the reconstructed ENSO indices. These predictions make it possible to reconstruct APCs, but as an expected value they also underestimate the true variance of each APC. Extreme APC

values (and the extreme SWLs they might prompt) are of particular interest for modeling coastal flood risk. So, it is critical to model and propagate the variance of regression residuals (Mukhopadhyay et al., 2018; Razavi et al., 2016). The choice of residual error model plays an important role, especially if there is low-frequency variability in the residuals not captured in the regression. Here, we apply a Wavelet autoregressive model (WARM; Kwon et al., 2007) to quantify and propagate residual variance and low-frequency periodicities into our final reconstructions of the APCs (see Appendix A1 for more detail). We add the simulated time series of APC residuals to the regression-generated APC estimates to generate final APC reconstructions.

The full length of the reconstruction is set to the length of the longest ENSO reconstruction used to predict the APCs (back to 1500 CE in this study). For the APCs that are reconstructed with shorter ENSO products (i.e., beginning later than 1500 CE), we only use simulations from the WARM model to fill in the period between 1500 CE and the start of the shorter ENSO products.

Using the APC reconstructions, we simulate three components of SWLs over the 1500–2000 period. First, simulations of η_{MMSL} are generated using the simulated APCs and Equation 2. These reconstructions emphasize the seasonal and monthly sea level anomalies driven by atmospheric variability linked to equatorial Pacific SSTAs. Second, an hourly deterministic simulated tide component (η_{Tide}) is added to the η_{MMSL} reconstructions. Lastly, simulated time series of η_{SS} are added to the reconstructions to generate 1,000, 500 yr traces of SWL time series at an hourly time step.

3.2.1. Variability in η_{MMSL}

The reconstructions of η_{MMSL} are assessed separately from the simulations of SWL to isolate the effects of slowly evolving sea level variations on extreme water levels from the effects of other SWL components. We use a quasi-stationary extreme value analysis (Wahl & Chambers, 2015) to understand the variability of η_{MMSL} over the last 500 yr. In this analysis, we first identify the annual maxima series (AMS) of η_{MMSL} in each 500 yr simulation. Then, using sliding windows of size w (with w = 100 or 30 yr), we estimate the magnitude of the 100 yrevent based on a GEV distribution fit to the AMS within the window via maximum likelihood. The window is moved 1 year at a time across the entire reconstruction period (1500–2000). We note that results are not sensitive to the choice of return period.

The time series of 100 yr events is calculated for each of the 1,000 stochastic traces of η_{MMSL}, resulting in an ensemble that quantifies uncertainty in this statistic through time due to natural variability linked to the ENSO reconstructions and additional noise from the ENSO regressions and TESLA model. We compare the variance in the 100 yr event across this ensemble to the uncertainty in the 100 yr event estimate based on uncertainty in the GEV fit. That is, we calculate the sampling variability in the 100 yr event using the Delta method (Coles, 2001) for each trace and each w-year sliding window, and then report the average confidence interval width from all GEV estimations.

3.3. Variability in Extreme SWLs and Its Components Due To Natural Variability and SLR

After assessing η_{MMSL} in isolation, we evaluate the variability in SWLs and all its components due both to natural variability and SLR. First, we separate the effects of natural variability from SLR on the SWL simulations by considering three conditions. Time series for condition 1 are directly obtained using TESLA, which incorporates observed SLR of 0.0022 m/yr starting in 1900 (for a total of 0.2 m of SLR by 2000). In condition 2, time series of SWLs do not contain an SLR component, so that they only reflect natural variability in the component time series. These time series are created by removing the linear SLR from SWLs in condition 1 between 1900 to 2000. In condition 3, SWL time series reflect a total of 0.2 m SLR applied over the entire length (500 yr) of SWL simulations, such that they combine the full range of natural variability in condition 2 with SLR experienced by 2000. The condition 3 represents a situation when we have (500 × 1,000) simulations of the SWL time series at the year 2000 CE with the total SLR of 0.2 m, such that this time series it accounts for larger extent of natural variability in the system informed by 500 yr of reconstruction. This does not decrease the SLR, rather it extends our understanding of the randomness or natural variability in the system. All three conditions are developed by updating η_{Tide}, while η_{MMSL} and η_{SS} remain unchanged.

For each of these three conditions, we examine the probability distribution of AMS across all 1,000 simulations and compare the water levels with flooding thresholds for San Francisco. We use four flooding thresholds for this purpose, as shown in Table 2. The minor, moderate, and major flooding thresholds are prescribed by Sweet

Table 2
Flooding Thresholds at the San Francisco Tide Gauge (9414290) Location

Flooding threshold (source)	Water levels, *m* above mean higher high water	Water levels, *m* above MSL
Nuisance Flooding (NOAA)	0.35	1.179
Minor (Sweet et al., 2022)	0.571	1.4
Moderate (Sweet et al., 2022)	0.853	1.68
Major (Sweet et al., 2022)	1.24	2.07

et al. (2022). All threshold values are converted to water levels above MSL at the San Francisco tide gauge location (0.95 m) assuming Mean Higher High Water at this gauge is 1.78 m, both relative to the same Mean Lower Low Water tidal datum (https://tidesandcurrents.noaa.gov/stationhome.html?id=9414290).

We then focus on the annual maxima that exceed the moderate flooding threshold under condition 3 (which combines natural variability and 0.2 m of SLR) and explore the fractional contribution of SWL components (η_{MMSL}, η_{Tide}, and η_{SS}) to these large flooding events. The choice of condition 3 and moderate flooding are selected for demonstration, but the analysis could be extended to any other flooding threshold and conditions of interest. We first calculate the component-wise average contribution to total SWL during moderate flooding events. Then, we calculate the joint likelihood of SWL components during moderate flooding events to understand which of the three SWL components more often or less often drive moderate flooding events, and how the roles of different components change as the magnitude of the SWL events become more extreme. These joint likelihoods are calculated in two different ways using trivariate empirical copulas (Nelsen, 2007, Zhang & Singh, 2019; see Appendix A2 for detail):

1. "OR" case: joint likelihood of at least one of the SWL components being greater than their respective moderate flooding thresholds (see Appendix A2 and Equation A4).
2. "AND" case: joint likelihood of SWL components all simultaneously being greater than their respective moderate flooding thresholds (see Appendix A2 and Equation A5).

In both "OR" and "AND" cases, the moderate flooding thresholds of SWL components are calculated as the quantiles of SWL components when hourly SWL crosses the moderate flooding threshold (as in Table 2). Among these moderate flooding events, we select more likely (smaller) and less likely (larger) events based on their probability of joint occurrence, and then report the non-exceedance probabilities of individual empirical marginals of η_{MMSL}, η_{Tide}, and η_{SS}. These empirical marginals show how the contributions of different components to SWL change as the magnitude of the SWL events become more extreme.

SWL emulation in TESLA is carried out using the open source codes on GitHub page https://github.com/teslakit/teslakit with modifications necessary for the present work. Reconstructions of APCs and SWLs from 1500 to 2000 CE and the results of the quasi-stationary flood risk analysis are publicly accessible at Mukhopadhyay et al. (2022). All statistical analyses are carried out with R (R Core Team, 2021) programming language.

4. Results

4.1. Validation and Reconstruction of SSTA APCs

Based on a stepwise regression (see Figures S2–S4 in Supporting Information S1), we select the following ENSO predictors for each of the APCs in Hovmöller space (bolded in Table 1): (a) the Niño 3.4 index described by Li et al. (2013) for APC_1, hereafter simply referred to as Niño 3.4, (b) the NCT for March–April-May (MAM) from Freund et al. (2019) for APC_2, (referred to as NCT_{MAM}) and (c) the NCT index for September–October–November (SON) from Freund et al. (2019) for APC_3 (referred to as NCT_{SON}). These covariates explain 53%, 5%, and 40% of variability in APC_1, APC_2, and APC_3, respectively. The Niño 3.4 index for APC_1 is based on a network of 2,222 tree-ring chronologies from both tropical and mid-latitude regions and captures canonical ENSO variability over the past 700 yr (1301–2005), including extended periods of La Nina during the little ice age and El Niño during the late twentieth century (Li et al., 2013). The NCT_{SON} index for APC_3, based on corals and sclerosponges, is designed specifically to capture ENSO activity in the western equatorial Pacific in the fall, but extends over a shorter period of 1617–2008. APC_2 cannot be well represented by any of the ENSO reconstructions available, with the best (NCT_{MAM}) still providing a poor fit. Additional analysis (not shown) suggests that APC_2 is also not well correlated with SSTAs outside of the tropical Pacific.

Figure 3 shows the coupled linear regression-WARM model performance in simulating APC_1. Figure 3a shows the cross-validated R^2 between historical APC_1 and out-of-sample predictions based on the Niño 3.4 index. The global wavelet power spectrum of the residuals (ϵ_1) of APC_1 regression estimates are shown in Figure 3b. There

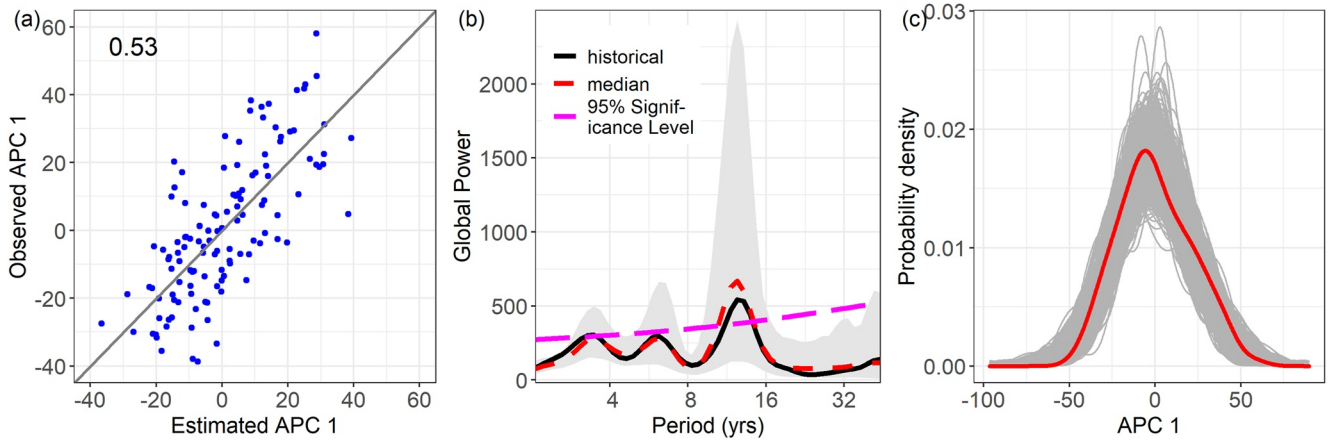

Figure 3. Linear model results for APC_1 (a) comparison between observed and estimated APC_1 from linear model using five-fold cross-validation test with cross-validated R^2 for each fold, (b) global power spectrum of residuals from linear model estimate of APC_1. The shaded region denotes the 5th and 95th percentiles of the wavelet spectra from the 1,000 WARM simulations, (c) probability density function of observed APC_1 (red) and the 1,000 simulations (gray).

is significant low-frequency variability at 3, 6, and 13 yr periodicities in the residuals. The WARM model uses these frequencies to decompose and simulate the residuals, recreating these same signatures (Figure 3b). WARM model residual simulations are added back to the regression estimated APC_1 to generate APC_1 simulations, which match the observed distribution of APC_1 (Figure 3c). Similar results for APC_2 and APC_3 are shown in Figures S6 and S7 in Supporting Information S1.

APC simulations and their power spectra are shown for all three APCs in Figure 4. Figures 4a, 4c, and 4e show historical versus median simulated APCs derived using the coupled linear regression-WARM model, with the gray bars indicating 95% confidence bounds across the 1,000 traces of simulated APCs. We report the cross-validated R^2 between the historical APCs and their out-of-sample predictions based on the Niño 3.4, NCT_{MAM}, and NCT_{SON} indices, respectively. The cross-validated R^2 values indicate the performance of each linear model only. In Figures 4b, 4d, 4f, we show the global wavelet spectrum of the simulated APCs for the historical (121 yr) period, rather than the spectrum of regression residuals (as was shown for APC_1 in Figure 3). That is, Figures 4b, 4d, 4f highlight the low-frequency variability present in the final reconstructions of each APC.

As highlighted earlier, APC_1 and APC_3 are predicted well, but not APC_2. Importantly, though, the simulations of APC values show a significant amount of variability around their conditional expectations. For all APCs, this variability manifests across scales, and it is well captured by the coupled linear regression-WARM model. APC_1 observations exhibit a significant peak power at around 6 yr and two secondary but insignificant peaks around 3 and 13 yr (Figure 4b). The APC_1 simulations capture the peak 6 yr signal but overestimate the secondary 13 yr peak, albeit with substantial uncertainty. APC_2 exhibits a substantial peak with a 7 yr periodicity, which the WARM model reproduces very well (Figure 4d). Little of this signal is captured by the ENSO regression. APC_3 exhibits a significant 3 yr peak and a smaller, insignificant peak at 6 yr (Figure 4f). These are reasonably well captured by ensemble of linear regression-WARM model simulations.

4.1.1. Natural Variability in Reconstructions of η_{MMSL}

The 1,000 traces of simulated APCs for 1500–2000 (Figures S8–S10 in Supporting Information S1) are used to drive the TESLA model, generating 1,000 traces each of hourly η_{MMSL}, η_{Tide}, and η_{SS} and thus SWL time series. We first focus on the reconstructions of η_{MMSL}. Figure 5a shows the median and 95% bounds of the AMS of η_{MMSL} across the 1,000 traces. The interannual variability in the AMS closely follows the variations in the ENSO predictors (Figures 5b–5d), especially the Niño 3.4 index that drives APC_1 (Figure 5b). Both η_{MMSL} AMS and the Niño 3.4 index exhibit significant variability and frequent peaks during the 20th century and a dearth of events during the 16th century. This is consistent with past work showing sensitivity of high tide and major flooding to the El Niño events across the U.S. West Coast (e.g., Sweet et al., 2018).

Figure 6 shows variability in the 100 yr flood event for η_{MMSL} based on a sliding 100 yr window (Figure 6a) and 30 yr window (Figure 6c) applied to each of the 1,000 traces. The sampling uncertainty associated with a fitted GEV model to 100 yr of data is also shown for comparison (blue error bar). Figures 6b and 6d show the coefficient

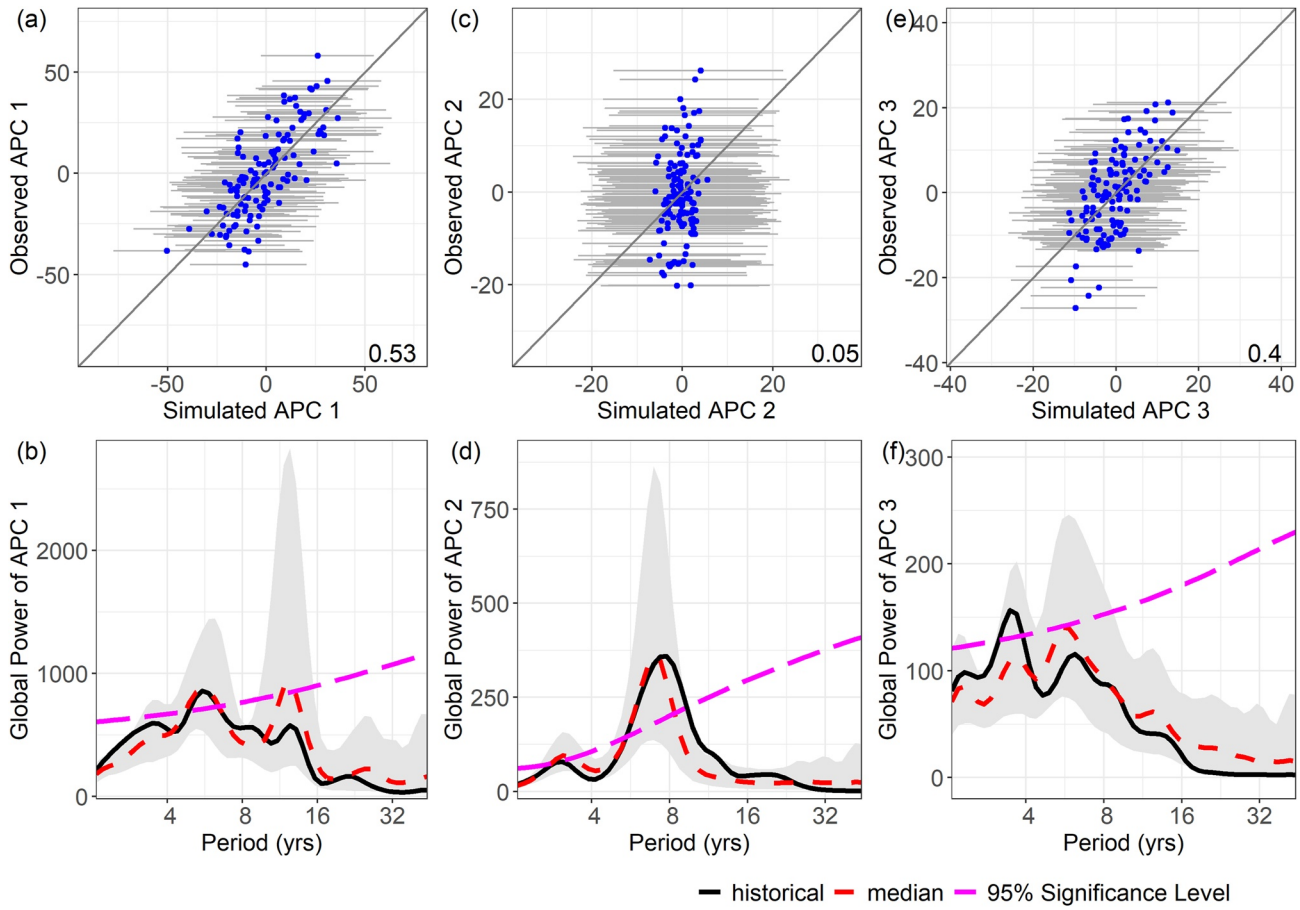

Figure 4. (a, c, e) Comparison between observed and simulated annual principal components (APCs) for 121 yr. Out-of-sample cross-validation R^2 between observations and predictions are also shown. (b, d, f) The global power spectrum of the observed APCs (black) and the mean global power spectrum of 1,000 WARM-simulated time series (red), along with a 95% significance level based on a red noise background process (pink).

of variation in the 100-year event across sliding windows, expressed as a distribution across the traces for each window size.

Several major features emerge from Figure 6. First, when using the 100 yr window, the median value across the 1,000 traces does not change significantly during the 500 yr period, exhibiting only a slight increase in the earliest part of the 16th century (Figure 6a). The lack of variability in the median is unsurprising, because the 100 yr window smooths out ENSO-induced variability that tends to manifest at inter-annual to decadal (rather than centennial) scales. In addition, the uncertainty in the 100 yr event for η_{MMSL} across the ensemble of traces is similar in size to the sampling uncertainty associated with a fitted GEV model to 100 yr of data (i.e., the width of the gray area is similar to the width of the blue error bars). This suggests that the simulation-based approach to uncertainty quantification aligns well with that estimated using more traditional statistical techniques.

In Figure 6a, the uncertainty bounds for the 100 yr events across the 1,000 traces appear relatively stable. However, this belies a significant degree of decadal-to-centennial variability in the 100 yr event for each of the 1,000 traces, which stems not only from the ENSO-based reconstructions but also the low-frequency variability captured by the WARM models. This is seen in Figure 6a using three randomly selected traces of the 100 yr event for η_{MMSL} (gray dotted lines). Notably, each of the three traces exhibit more variability in the 100 yr event than the median value across the ensemble (red line). Figure 6b shows the coefficient of variation in the 100 yr event across all 1,000 traces, and further emphasizes that the variability in the 100 yr event for each trace is significant in comparison to its median value.

This result becomes even more apparent if the window used to estimate the 100 yr event is shorter. Figures 6c and 6d is the same as Figures 6a and 6b, but based on 100 yr events estimated from a sliding 30 yr window. With

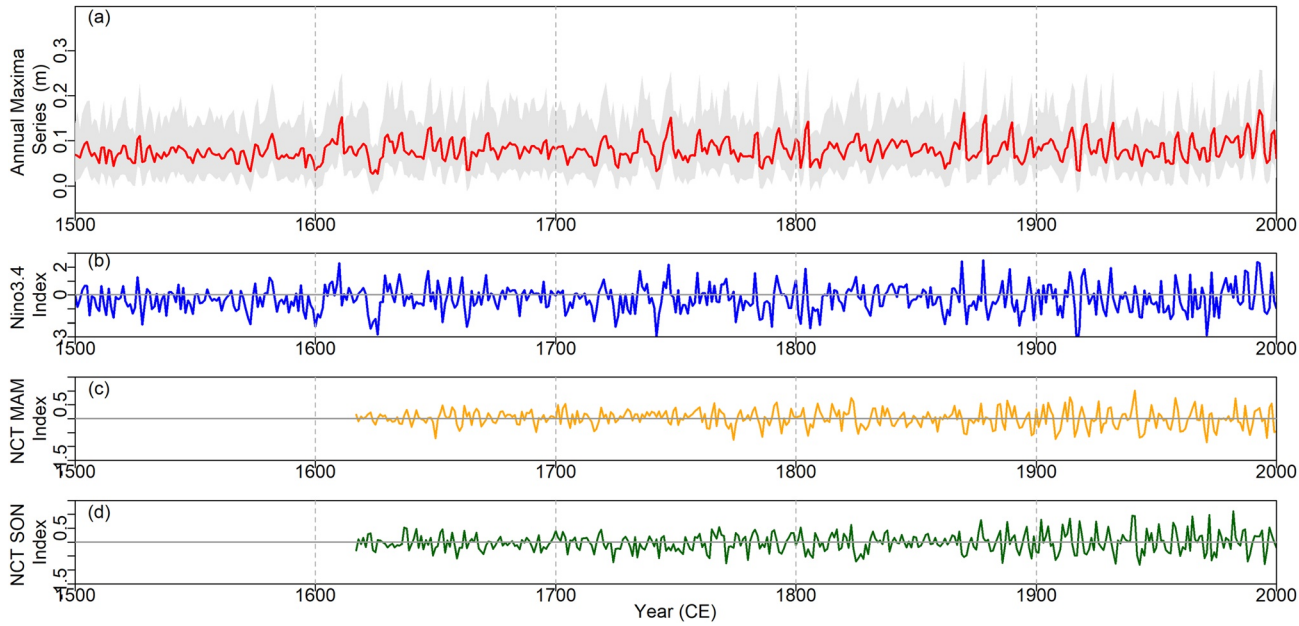

Figure 5. Flood risk analysis using η_{MMSL}: (a) Times series of annual maxima η_{MMSL} . Red line shows median of 1,000 simulations with 95 percentile range shown by the gray shaded region. (b) Niño 3.4 index from Li et al. (2013). (c) NCT_{MAM} index from Freund et al. (2019). (d) NCT_{SON} index from Freund et al. (2019).

a shorter window, not only do individual traces exhibit more variability in the 100 yr event estimate, but the median 100 yr event estimate also varies across the centuries. Within this shorter window, ENSO variability is significant enough so that many traces within the ensemble exhibit the same fluctuations, driving changes in the median estimate. In Figure 6c, sampling uncertainty in a GEV model (the blue error bar) covers only about half of the total ensemble uncertainty in the 100 yr events for the η_{MMSL} reconstructions in certain centuries, and the coefficients of variation across traces can reach upwards of 40%.

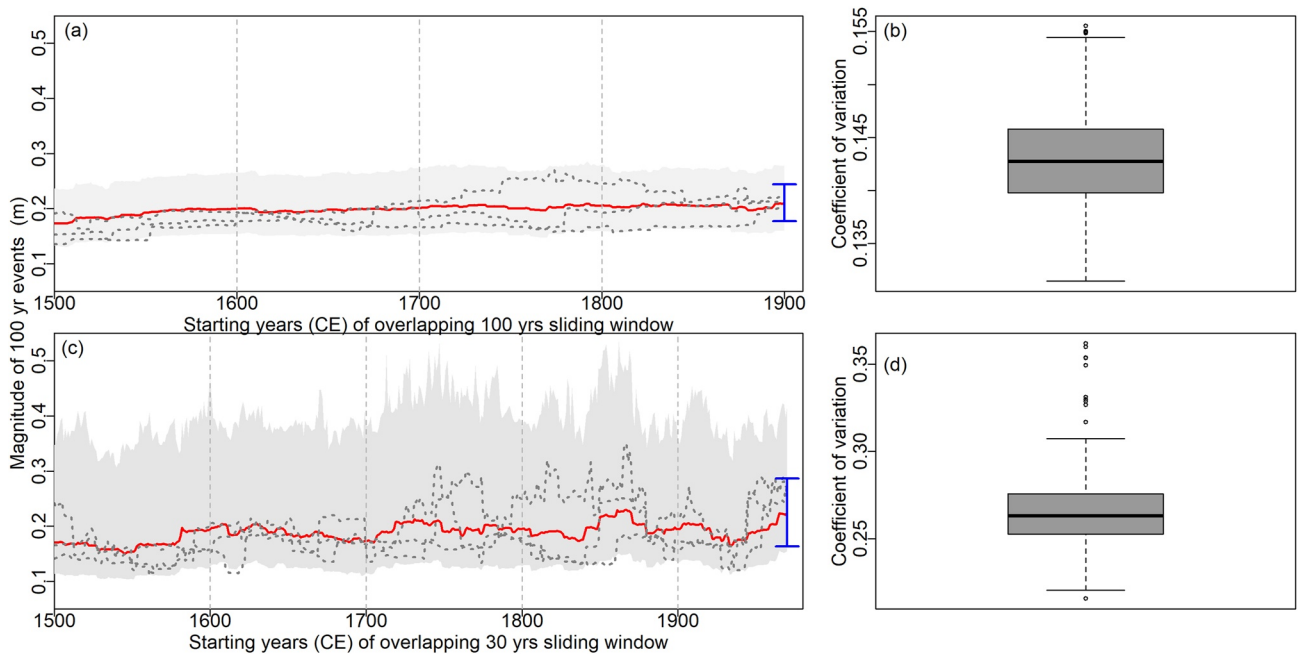

Figure 6. (a) Example of individual η_{slow} traces out of 1,000 simulations that exhibit significant variability in 100 yr events. Red line shows median 100 yr events of 1,000 simulations with 95 percentile range shown by the shaded region. Average sampling variability from generalized extreme value fit is shown by error bar (blue). (b) Coefficient of variations across 100 simulations. (c, d) Same as (a, b) but 100 yr events estimated from 30 yr sliding window.

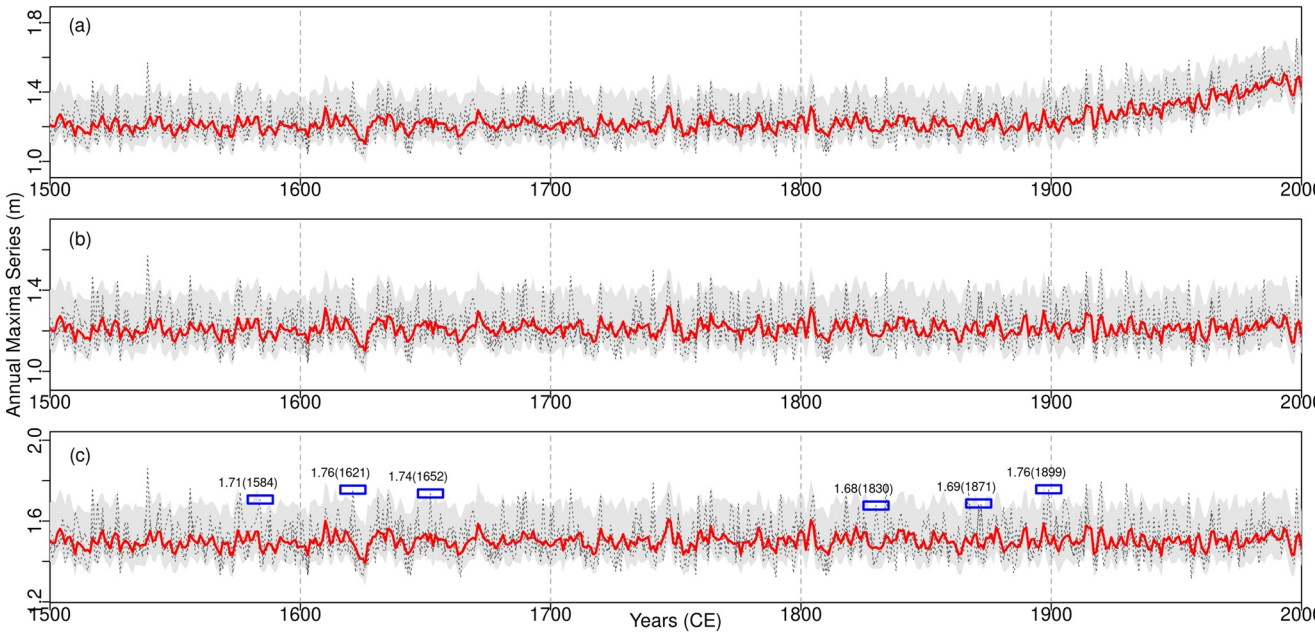

Figure 7. Flood risk analysis using still water level (SWL) ($\eta_{MMSL} + \eta_{tide} + \eta_{SS}$): (a) with sea level rise (SLR) after 1900, and two synthetic annual maxima SWL considering (b) no SLR and (c) a total of 0.2 m SLR for entire 500 yr. Red line shows median of 1,000 simulations (shaded region shows 95% interval). Gray lines are three randomly sampled traces from simulations. For each trace, two extreme events over 97.5th percentiles are shown as SWL annual maxima values (year of occurrence).

The results in Figure 6 have important implications, because the design of coastal flood infrastructure is often based on a single trace of TWLs (i.e., the observed record), and the results here suggest that one component (η_{MMSL}) of TWLs over a single trace can vary substantially on multi-decadal timescales. Therefore, data collected over a short period (e.g., 30 yr) may poorly reflect the range of natural variability possible in extreme events of η_{MMSL}, and this issue may still not be fully resolved with a 100 yr record. For context, Figure 6a suggests decadal-to-centennial scale variation of about 15 cm in the 100 yr event of η_{MMSL} when using a 100 yr sliding window, while these variations grow to 40 cm when using a 30 yr sliding window (Figure 6c). These variations could have larger impacts to that of mean SLR over a 20–30-yr period (assuming a projected 2–3 mm/yr rate for the U.S. West Coast; Sweet et al., 2022).

4.2. Variability in SWLs Due To Natural Variability and SLR

Figure 7 introduces the three conditions of SLR and natural variability discussed in Section 3.4. Figure 7a shows the AMS series of SWL reconstructions from 1500 to 2000 for condition 1. The effect of SLR of 0.0022 m/yr occurring since 1900 is evident from the gradual increase in annual maxima from 1900 forward. Figure 7b shows the AMS SWL for condition 2 that removes SLR from SWLs, and Figure 7c shows the effects of 0.2 m of SLR added to all 500 yr of simulation (condition 3). There is large annual to decadal variations in the AMS, which is consistent with the findings in Figure 5. The combined effect of SLR and natural variability is evident in the increased median AMS SWL in Figure 7c compared to Figures 7a and 7b.

The probability density functions for AMS SWL are shown in Figure 8 for each of the three conditions, along with flooding thresholds at the tide gauge. The overall shift in water levels from nuisance flooding toward minor flooding are evident once SLR is considered across the entire simulation (i.e., condition 3). There is also a considerable number of AMS SWL values above the moderate flooding threshold under condition 3, consistent with previous studies examining high tide flooding in San Francisco with SLR (Sweet et al., 2018, 2022). Between conditions 1 and 3, the likelihood of minor flooding (1.4 m above MSL) increases from 8.6% to 93.5%. Most notably, between conditions 1 and 3, the likelihood of moderate flooding (1.68 m above MSL) grows from 0.001% to 3.6%. We argue that this increase in flood risk is the result of accounting for the full extent of natural variability over the last 500 yr.

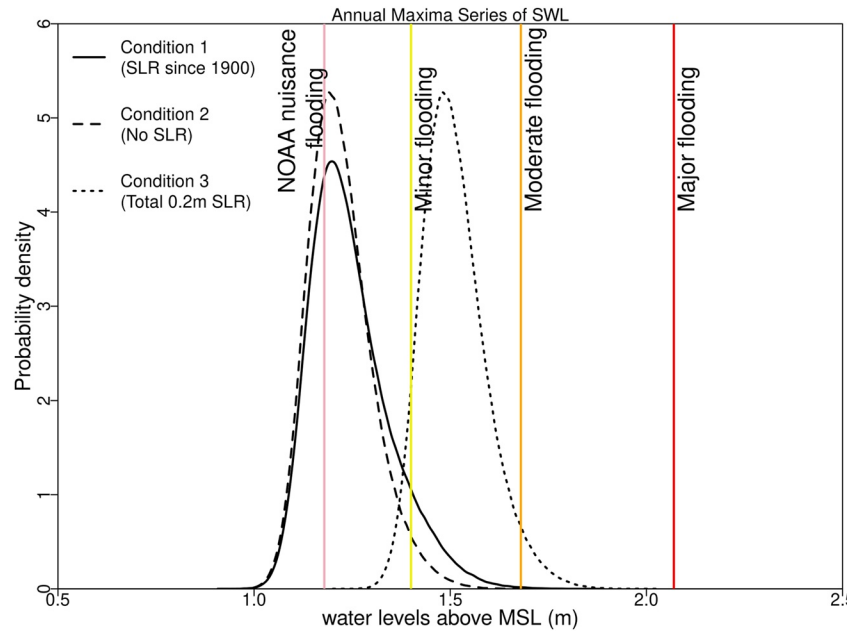

Figure 8. Probability density functions of annual maxima still water level (SWL) for three conditions: (a) condition 1: with sea level rise (SLR) after 1900; (b) condition 2: no SLR; and (c) condition 3: a total of 0.2 m SLR for the entire 500 yr simulation.

The ensemble simulations for condition 3 allow us to investigate the combined effect of SLR and natural variability in SWL more reliably, as well as the contribution of individual components to total flooding magnitude. First, we highlight a few randomly selected moderate flooding events for a randomly selected trace under condition 3 to explore how the components (η_{MMSL}, η_{Tide}, and η_{SS}) combine to lead to moderate flooding in SWLs (see blue boxes in Figure 7c). Figure 9 shows the hourly time series of these components for one event (similar results for other events are shown in Figures S11–S15 in Supporting Information S1). Figure 9 shows an anomalously high value of η_{MMSL} occurring simultaneously with above average η_{Tide} and a peak in η_{SS}. When looking at multiple such events (Figures S11–S15 in Supporting Information S1), it becomes clear that a diverse combination of η_{MMSL}, η_{Tide}, and η_{SS} values can result in moderate flooding, with not all peaking simultaneously. This suggests the need for a more careful assessment of the contributions and joint likelihoods of SWL components during moderate flooding events.

Figure 10a shows the average contribution of hourly values of η_{MMSL}, η_{Tide}, and η_{SS} across all events where hourly SWL cross the moderate flooding threshold for all simulations under condition 3. On average, η_{MMSL}, η_{Tide}, and η_{SS} contribute 5.7%, 78.5%, and 15.8% of the SWL during these events. The large contribution of η_{Tide} emphasizes that moderate flooding is really only possible at high tide, consistent with the findings from Serafin and Ruggiero (2014). Also, storm surge appears to contribute three times as much to moderate flooding water levels as compared to slower variations in MMSLAs.

The joint likelihood of occurrence of at least one of η_{MMSL}, η_{Tide}, and η_{SS} exceeding the values experienced during a moderate flooding event is shown in Figure 10b, following the "OR" case discussed in Section 3.4. Probabilities on the *y*-axis in Figure 10b are calculated using Equation A4 and plotted against hourly SWL magnitudes during moderate flooding events. Figure 10b shows that as the magnitude of moderate flooding becomes more intense, the probability of having at least one of η_{MMSL}, η_{Tide}, and η_{SS} exceeding its value during that event declines. This is consistent with the idea that larger moderate flooding events will be less likely. Among these events, we pick more likely events based on an "OR" joint likelihood of 20% or more (blue shaded region in Figure 10b), and less likely events based on a joint likelihood of 5% or less (orange shaded region). For both the more and less likely events, we plot the marginal non-exceedance probabilities for η_{MMSL}, η_{Tide}, and η_{SS} in Figures 10c and 10d, respectively. These non-exceedance probabilities in the marginal illustrate which of the three components are consistently at the upper end of their range during more or less likely moderate flooding events, and which components exhibit more variability in magnitude during these events.

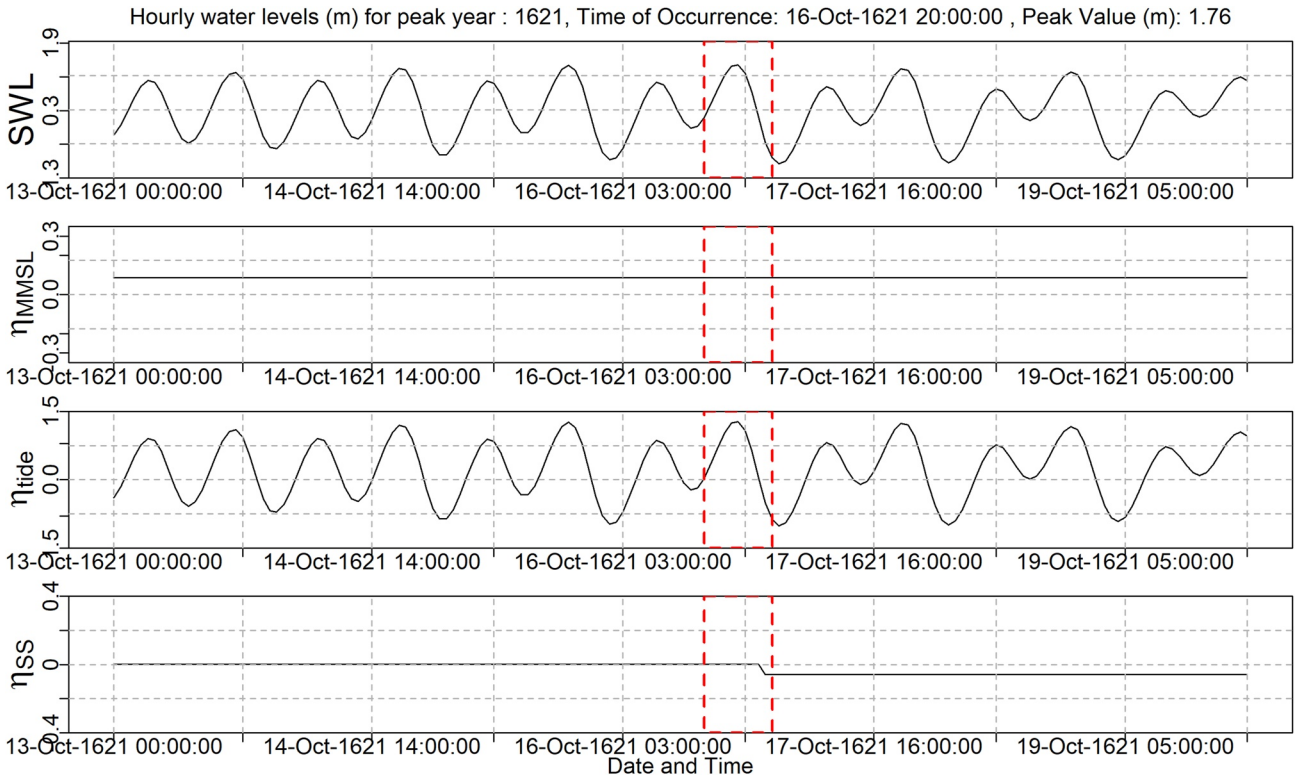

Figure 9. Components of hourly still water level (SWL) during peak SWL in 1621 for condition 3.

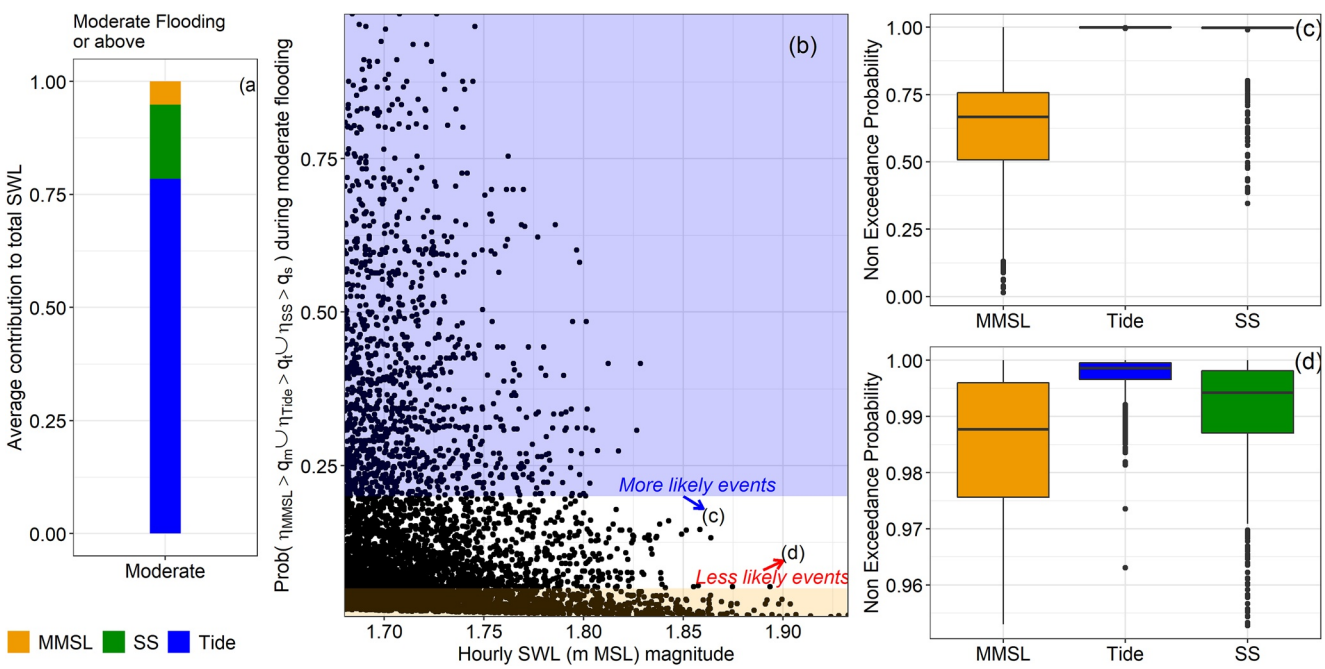

Figure 10. (a) Average contribution of three component time series to daily max still water level (SWL) by magnitude, (b) join probability of occurrence $P(\eta_{\mathrm{MMSL}} > q_m \cup \eta_{\mathrm{Tide}} > q_t \cup \eta_{\mathrm{SS}} > q_S)$ for "OR" case during each moderate flooding event. The non-exceedance probabilities of SWL components during (c) more likely flooding events and (d) less likely flooding events. q_m, q_t, and q_S are the η_{MMSL}, η_{Tide} and η_{SS} values experienced during a moderate flooding event respectively.

For the more likely events (Figure 10c), both tide and storm surge levels are consistently toward the upper end of their range during these events. Conversely, η_{MMSL} varies much more greatly across its range during these events, suggesting that more likely moderate flooding events (which are often smaller in magnitude) can be generated with a wide range of η_{MMSL} provided that η_{Tide} and η_{SS} are near their maximum values.

In contrast, during less likely (and often larger) moderate flooding events (Figure 10d), the range of variability in all three components is compressed toward the upper end of the distribution (i.e., above their 95th percentiles). That is, to generate the less likely and often larger moderate flooding events in SWL that approach the major flooding threshold (2.07 m), it requires that tide and storm surge reach the upper tails of their distribution *and simultaneously* that slower variations in MMSLs do the same. We note that these results are consistent when using the "AND" joint likelihood in Equation A5, although the overall joint probabilities are lower (see Figure S16 in Supporting Information S1).

5. Discussion and Conclusion

Although multiple processes influence coastal flooding, ESL is sensitive to ENSO phase along the U.S. Pacific Coast (Menéndez & Woodworth, 2010; Sweet & Park, 2014). Our reconstructions suggest a strong relationship between non-tidal, slowly evolving anomalies in mean monthly sea levels and ENSO phase. In particular, the AMS of η_{MMSL} reconstructions follow interannual to decadal scale variations in ENSO events consistent with previous studies (Serafin et al., 2017; Sweet & Park, 2014), and also exhibit small shifts during the little ice age and increased Niño 3.4 activity in the 20th century. The spatio-temporal shifts in ENSO over the Pacific during the latter half of the twentieth century are accounted for in our modeling using the predictors NCT_{MAM} and NCT_{SON}. NCT_{SON} in particular represents ENSO activity in the western equatorial Pacific in the fall (Freund et al., 2019), which is consistent with APC_3 being described as an eastward propagating Kelvin wave during boreal summer and fall (Anderson et al., 2019). The linear models explain 56% and 38% of variance in the conditional mean of APC_1 and APC_3 using their respective ENSO predictors, but overall low-frequency periodicities of all APCs are well captured using WARM simulations. Purely regression-based methods using modes of variability can only partially address the uncertainties from natural variability, particularly in tide gauge observation-based studies (Sweet et al., 2022). The coupled linear regression-WARM framework presented here shows a promising alternative for ENSO-based reconstructions of tide gauge records, as it provides an effective approach for accounting for natural variability in water levels at different coastal locations.

The highly stochastic nature of the slowly evolving monthly and seasonal sea level anomalies, linked to synoptic weather conditions, reveals that longer record lengths are essential for reliable estimation of design levels and their uncertainty. Our results show that variations in slowly evolving MMSLs can have a larger impact than SLR of 2–3 mm/yr over 20–30 yr. In addition, the ensemble uncertainty in estimates of the 100 yr return level of η_{MMSL} is significantly larger when record lengths are reduced from 100 to 30 yr, and also exceeds the uncertainty that would be estimated using more traditional statistical approaches (e.g., uncertainty bands from a fitted GEV distribution to annual maxima). These results emphasize that reliable estimates of extreme sea water levels need long observational records, and that great care is needed in selecting design events when based on data that only span a few decades (Lang et al., 2019; Moftakhari et al., 2015; Wahl & Chambers, 2015; Wahl et al., 2017).

Our results show that when the effects of 0.2 m of SLR and natural variability in SWLs are combined, there is a large increase in the occurrence of moderate flooding events in the San Francisco Bay. Estimating the probability of these floods is difficult if based only on the most recent sea level records that contain recent levels of SLR, because they lack a full representation of natural variability in SWL components. The approach presented in this work addresses this challenge. Even without considering wave- and river-driven water levels, the increases in moderate flood risk could be very detrimental to the San Francisco Bay coastal infrastructure. This increase in flood risk further emphasizes the need to account for these changes due to the natural variability of coastal water levels in future coastal development.

For San Francisco Bay, extreme SWLs are tidally dominated, as opposed to the east coast where contributions of non-tidal components such as storm surges are typically dominant in extreme sea levels (Sweet et al., 2018). Our findings confirm this result, but also show that contributions of non-tidal factors to low-probability extremes in the West cannot be neglected (Serafin et al., 2017). In particular, we find that variations in η_{MMSL} can act as a dominant factor in the tails of coastal flooding events in the San Francisco Bay. While smaller flooding events

are primarily dominated by high tide coupled with storm surge, the largest events require that positive anomalies in η_{MMSL} synchronize with tides and storm surges. This suggests the potential to improve subseasonal-to-seasonal forecasts of major coastal flood risk based on forecasts of η_{MMSL}, which can be improved with more advanced ENSO forecasts.

A few limitations of this work require discussion and could suggest important avenues for future work. First, the simulation of tide data with present MSL could, however small, be a source of error and needs to be further explored. Nonlinear interactions between storm surges, MMSLs, and tides are not accounted for in our linear superposition approach (Equation 1) and can lead to additional error. Furthermore, this work did not account for the impact of wave or river driven water levels given the nature of the study site location, but additional work should expand this approach to consider all components of TWLs. We also note that although there is clear evidence of a shift in coastal water levels above minor and moderate flooding thresholds when SLR and natural variability are combined, the uncertainties from different modeling components can obscure SWL comparisons with strict flooding thresholds.

In this work, we only reconstruct annual scale proxies for sea level variability from the tropical Pacific, while other atmospheric and oceanographic inputs that are incorporated in TESLA (e.g., MJO, local SLP predictors) that are sub-seasonal or more localized, are reconstructed based on the initial APC reconstructions. Future work should develop paleo-proxy based reconstructions for these other climatic and oceanographic drivers to further inform the water level emulator. Further investigations can be carried out to understand the effects of extra-tropical climate modes (e.g., Pacific Decadal Oscillation) on coastal sea level variability and the need for expanding the current framework to consider paleo-proxy reconstructions for those modes. In addition, the computationally efficient framework presented in this work should be expanded to better understand the combined impacts of SLR and natural water variability on coastal flood risk beyond the West Coast. However, future work would be required to identify relevant paleo-proxies for slowly evolving water levels beyond the Pacific.

6. Conclusions

This study contributes a novel approach to couple paleo-proxy reconstructions of equatorial SSTAs with coastal water level emulation to better understand natural variability in still water level and its components at interannual-centennial timescales. We developed a coupled linear regression-WARM framework to utilize several paleo proxy-based ENSO reconstructions to inform a modified version of the TESLA coastal water level emulator and generate stochastic reconstructions of water levels since 1500 CE. Using the San Francisco (USA) tide gauge for demonstration, we analyzed the combined effect of sea level rise and natural variability on extreme still water level and its components. The primary conclusions of this work are as follows.

- ENSO variability significantly impacts slowly evolving mean monthly sea level anomalies along the Western U.S. coast, and these variations can impart large sampling variability into the estimation of design events (e.g., 100 yr flood) if record lengths are short (<30 yr).
- The combined effect of natural variability in mean monthly sea level anomalies, storm surge, tide, and sea level rise can substantially increase the likelihood of large coastal flood events, well beyond what recent observations suggest.
- With sea-level rise, a diverse combination of still water level components can lead to coastal flooding events. However, low-magnitude coastal flooding is most often driven by the simultaneous occurrence of high tide and large storm surges, while high-magnitude flooding requires the simultaneous occurrence of high tide, large storm surges, and anomalously high monthly sea level anomalies.

Appendix A

A1. Wavelet Autoregressive Model for APC Residuals

In this study, we apply a Wavelet autoregressive model (WARM; Kwon et al., 2007) to quantify and propagate residual variance and low-frequency periodicities into our final reconstructions of the APCs. The residuals $\epsilon_{t,i}$ in Equation 3 are modeled by first decomposing them into H orthogonal component series representing low frequency signals and a noise component (ν_t).

$$\epsilon_{t,i} = \sum_{h=1}^{H} Z_{h,t,i} + \nu_{t,i}, i = 1, 2, 3 \quad \text{(A1)}$$

This decomposition is based on the wavelet spectrum of $\epsilon_{t,i}$ (using the Morlet wavelet). From that spectrum, we identify H frequency bands of low-frequency variability where the global variation is significantly different from a background red-noise process (at the 95% significance level). The J scales of the wavelet spectrum $(a_{h_1}, \ldots, a_{h_J})$ that are significant for the hth frequency band are clustered together, and from those scales, a times series projection for the hth component $Z_{h,t}$ is estimated as the sum of the real part of the wavelet transform (note the subscript i for the ith APC has been dropped for simplicity):

$$Z_{h,t} = \sum_{j=1}^{J} Z_{h,t,j} = \frac{\delta_j \delta_t^{1/2}}{C_\delta \psi_0(0)} \sum_{j=0}^{J} \frac{R\left(W_t\left(a_{h_j}\right)\right)}{{a_{h_j}}^{1/2}} \tag{A2}$$

Here, C_δ is a wavelet function constant (0.776 for the Morlet wavelet), $\psi_0(0) = \pi^{-1/4}$ is the factor that removes energy scaling for the Morlet wavelet, $a_{h_j}^{1/2}$ converts the wavelet transform to an energy density function, and δ_i and δ_t are the scale-averaging coefficient and time-averaging factor, respectively. $R\{.\}$ denotes the real part of W, the wavelet transform of the residual time series $\epsilon_{t,i}$ at scale a_{h_j}.

For the i^{th} APC residual $\epsilon_{t,i}$, the decomposed time series $Z_{h,t,i}$ and the noise $\nu_{t,i}$ are then modeled stochastically using an autoregressive moving average (ARMA) model. Simulations from each ARMA model are summed to generate a trace of $\epsilon_{t,i}$ with the correct variance and low-frequency structure. To generate ensemble reconstructions of each APC, the following steps are used:

1. Estimate the conditional expectation of each APC based on the ENSO-based regressions in Equation 3 ($\widehat{\mathrm{APC}_i}$).
2. Using the WARM model, simulate $S = 1{,}000$ traces of residual time series for the same period as the APC reconstructions in step 1 ($\widetilde{\epsilon_{s,i}}$). Each simulation has a 121 yr burn-in period i.e., discarded to ensure simulations are not in-phase due to initial conditions.
3. Add the simulated time series of APC residuals $\widetilde{\epsilon_{s,i}}$ to the regression-generated APC estimates ($\widehat{\mathrm{APC}_i}$) to generate APC simulations ($\widetilde{\mathrm{APC}_{s,i}}$). Compare the statistical properties of these simulated time series to those in the observed APC time series.

A2. Joint Likelihood Estimation of SWL Components

We assess the joint likelihood of occurrence of the three SWL components during moderate flooding events through the following procedure:

1. We begin by constructing a trivariate empirical copula (Nelsen, 2007) of non-exceedance probabilities of hourly time series of $\eta_{\mathrm{MMSL}}, \eta_{\mathrm{Tide}}$, and η_{SS}. If the normalized ranked values of hourly series of $\eta_{\mathrm{MMSL}}, \eta_{\mathrm{Tide}}$, and η_{SS} are denoted as U, V, and W respectively, we construct the empirical copula (C_n) as:

$$C_n(u, v, w) = \frac{1}{n} \sum_{i=1}^{n} \begin{cases} 1 & \text{, if } \{U_i \le u, V_i \le v, W_i \le w\} \\ 0 & \text{, otherwise} \end{cases} \tag{A3}$$

   The sample size $n = T \times n.\mathrm{sim}$, where T is the total number of days in 500 yr and n.sim is the number of simulations, chosen here to be 1,000. The empirical marginals (u, v, w) are defined over the 3-dimensional domain $[0, 1]$. We also compute pairwise bivariate empirical copulas $C_{\mathrm{UV}}(u, v)$, $C_{\mathrm{UW}}(u, w)$, and $C_{\mathrm{VW}}(v, w)$. The pairwise copula formulations are similar to Equation A3 but for bivariate cases.
2. Next, to calculate the joint probability of occurrence of $\eta_{\mathrm{MMSL}}, \eta_{\mathrm{Tide}}$ and η_{SS} at the water levels corresponding to daily maximum SWLs above the moderate flooding threshold, we first take a subset (u^*, v^*, w^*) of (u, v, w) time series triplets by selecting the entries corresponding to SWL > 1.68 m above MSL. Then at these marginal triplets (u^*, v^*, w^*), we calculate the probabilities $C_{\mathrm{UV}}(u^*, v^*)$, $C_{\mathrm{UW}}(u^*, w^*)$ and $C_{\mathrm{VW}}(v^*, w^*)$ using the pairwise empirical copulas. We also calculate the joint probabilities $P(U \le u^*, V \le v^*, W \le w^*) = C_n(U_i \le u^*, V_i \le v^*, W_i \le w^*) = C_n(u^*, v^*, w^*)$.
3. Next, following Zhang and Singh (2019), we calculate two joint probabilities:
   (a) "OR" case: joint likelihood of at least one of the triplets (u, v, w) being greater than (u^*, v^*, w^*), as shown equation in Equation A4. In Equation A4, q_m, q_t, and q_S are the values of $\eta_{\mathrm{MMSL}}, \eta_{\mathrm{Tide}}$ and η_{SS}, respectively, during moderate flooding.

$$P(\eta_{\mathrm{MMSL}} > q_m \cup \eta_{\mathrm{Tide}} > q_t \cup \eta_{\mathrm{SS}} > q_S) = 1 - C_n(u^*, v^*, w^*) \tag{A4}$$

(b) "AND" case: joint likelihood of (u, v, w) all simultaneously being greater than (u^*, v^*, w^*), as shown in Equation A5.

$$\begin{aligned} P(\eta_{\mathrm{MMSL}} > q_m \cap \eta_{\mathrm{Tide}} > q_t \cap \eta_{\mathrm{SS}} > q_S) \\ = 1 - u^* - v^* - w^* + C_{\mathrm{UV}}(u^*, v^*) + C_{\mathrm{UW}}(u^*, w^*) \\ + C_{\mathrm{VW}}(v^*, w^*) - C_n(u^*, v^*, w^*) \end{aligned} \tag{A5}$$

The operator symbols '∪' and '∩' in Equations A4 and A5 denote union and intersection operations respectively.

Acronyms and Abbreviations

AWT	Annual weather type
APC	Annual principal component
MJO	Madden-Julian Oscillation
ENSO	El Niño Southern Oscillation
EVA	Extreme value analysis
GEV	Generalized extreme value
MMSL	Monthly mean sea level
PCA	Principal component analysis
PC	Principal component
SLR	Sea level rise
TWL	Total water level
SWL	Still water level
MMSLA	Monthly mean sea level anomaly
MSL	Mean sea level
ESL	Extreme sea level
TESLA	Time-varying emulator for short- and long-term analysis
CE	Common era
SLP	Sea level pressure
MPC	Monthly scale principal component
NOAA	National Oceanic and Atmospheric Administration
SSTA	Sea surface temperature anomaly
WARM	Wavelet Auto-regression model
AMS	Annual maxima series
NCT	Niño Cold Tongue
NWP	Niño Warm Pool

Data Availability Statement

Data set for this research is available in this in-text data citation reference: Mukhopadhyay et al. (2022) (with Creative Commons Attribution 4.0 International license, without any restrictions).

Acknowledgments
The authors thank Todd Steissberg, U.S. Army Corps of Engineers (USACE) Engineer Research and Development Center (ERDC) Environmental Laboratory, for his contributions enabling this research. This work was supported by the USACE, Institute for Water Resources and the Anticipating Threats in Natural Systems (ACTIONS) Congressional Interest project, USACE ERDC, Environmental Laboratory.

References

Anderson, D. L., Rueda, A., Cagigal, L., Antolinez, J. A. A., Mendez, F. J., & Ruggiero, P. (2019). Time-varying emulator for short and long-term analysis of coastal flood hazard potential. *Journal of Geophysical Research: Oceans*, *124*, 9209–9234. https://doi.org/10.1029/2019JC015312

Anderson, D. L., Ruggiero, P., Mendez, F. J., Barnard, P. L., Erikson, L. H., O'Neill, A. C., et al. (2021). Projecting climate dependent coastal flood risk with a hybrid statistical dynamical model. *Earth's Future*, *9*(12), e2021EF002285.

Arns, A., Wahl, T., Wolff, C., Vafeidis, A. T., Haigh, I. D., Woodworth, P., et al. (2020). Nonlinear interaction modulates global extreme sea levels, coastal flood exposure, and impacts. *Nature Communications*, *11*(1), 1–9.

Baek, S. H., Steiger, N. J., Smerdon, J. E., & Seager, R. (2019). Oceanic drivers of widespread summer droughts in the United States over the Common Era. *Geophysical Research Letters*, *46*(14), 8271–8280. https://doi.org/10.1029/2019GL082838

Barnard, P. L., Erikson, L. H., Foxgrover, A. C., Finzi Hart, J. A., Limber, P., O'Neill, A. C., et al. (2019). Dynamic flood modeling essential to assess the coastal impacts of climate change. *Scientific Reports*, *9*, 4309. https://doi.org/10.1038/s41598-019-40742-z

Barnard, P. L., Short, A. D., Harley, M. D., Splinter, K. D., Vitousek, S., Turner, I. L., et al. (2015). Coastal vulnerability across the Pacific dominated by El Niño Southern Oscillation. *Nature Geoscience*, *8*(10), 801–807.

Barnard, P. L., van Ormondt, M., Erikson, L. H., Eshleman, J., Hapke, C., Ruggiero, P., et al. (2014). Development of the Coastal Storm Modeling System (CoSMoS) for predicting the impact of storms on high-energy, active-margin coasts. *Natural Hazards*, *74*, 1095–1125.

Borkotoky, S. S., Williams, A. P., Cook, E. R., & Steinschneider, S. (2021). Reconstructing extreme precipitation in the Sacramento River Watershed using tree-ring based proxies of cold-season precipitation. *Water Resources Research*, *57*, e2020WR028824. https://doi.org/10.1029/2020WR028824

Cagigal, L., Rueda, A., Anderson, D., Ruggiero, P., Merrifield, M. A., Montaño, J., et al. (2020). A multivariate, stochastic, climate-based wave emulator for shoreline change modeling. *Ocean Modeling*, *154*, 101695.

Cagigal, L., Rueda, A., Ricondo, A., Pérez, J., Ripoll, N., Coco, G., & Méndez, F. J. (2021). Climate-based emulator of distant swell trains and local seas approaching a Pacific atoll. *Journal of Geophysical Research: Oceans*, *126*, e2020JC016919. https://doi.org/10.1029/2020JC016919

Calafat, F. M., Chambers, D. P., & Tsimplis, M. N. (2013). Inter-annual to decadal sea-level variability in the coastal zones of the Norwegian and Siberian Seas: The role of atmospheric forcing. *Journal of Geophysical Research: Oceans*, *118*(3), 1287–1301. https://doi.org/10.1002/jgrc.20106

Callaghan, D. P., Nielsen, P., Short, A., & Ranasinghe, R. W. M. R. J. B. (2008). Statistical simulation of wave climate and extreme beach erosion. *Coastal Engineering*, *55*(5), 375–390.

Chen, F., Xu, Q., Chen, J., Birks, H. J. B., Liu, J., Zhang, S., et al. (2015). East Asian summer monsoon precipitation variability since the last deglaciation. *Scientific Reports*, *5*(1), 1–11.

Codiga, D. L. (2011). *Unified tidal analysis and prediction using the UTide Matlab functions (Technical Report 2011-01)*(p. 59). Graduate School of Oceanography, University of Rhode Island. Retrieved from ftp://www.po.gso.uri.edu/pub/downloads/codiga/pubs/2011Codiga-UTide-Report.pdf

Coles, S. (2001). *An introduction to statistical modeling of extreme value*s. Springer-Verlag.

Cook, E. R., D'Arrigo, R. D., & Anchukaitis, K. J. (2008). ENSO reconstructions from long tree-ring chronologies: Unifying the differences? Talk presented at a special workshop on "Reconciling ENSO chronologies for the past 500 yr", held in Moorea, French Polynesia on 2–3 April 2008. Retrieved from https://www.ncei.noaa.gov/access/paleo-search/study/8704

Dangendorf, S., Calafat, F. M., Arns, A., Wahl, T., Haigh, I. D., & Jensen, J. (2014). Mean sea level variability in the North Sea: Processes and implications. *Journal of Geophysical Research: Oceans*, *119*(10). https://doi.org/10.1002/2014JC009901

Dätwyler, C., Abram, N. J., Grosjean, M., Wahl, E. R., & Neukom, R. (2019). El Niño-Southern Oscillation variability, teleconnection changes, and responses to large volcanic eruptions since AD 1000. *International Journal of Climatology*, *39*(5), 2711–2724.

de Souza, D. C., Ramos da Silva, R., Gomes da Silva, P., Fetter Filho, A. F. H., Mendez, F. J., & Werth, D. (2022). A hybrid regional climate downscaling for the southern Brazil coastal region. *International Journal of Climatology*, *42*(13), 6753–6770. https://doi.org/10.1002/joc.7607

Emile-Geay, J., Cobb, K. M., Mann, M. E., & Wittenberg, A. T. (2013). Estimating central equatorial Pacific SST variability over the past millennium. Part II: Reconstructions and implications. *Journal of Climate*, *26*(7), 2329–2352.

Emile-Geay, J., & Tingley, M. P. (2015). Inferring climate variability from nonlinear proxies: Application to paleo-ENSO studies. *Climate of the Past Discussions*, *11*(4).

Frederikse, T., Riva, R., Slobbe, C., Broerse, T., & Verlaan, M. (2016). Estimating decadal variability in sea level from tide gauge records: An application to the North Sea. *Journal of Geophysical Research: Oceans*, *121*(3), 1529–1545. https://doi.org/10.1002/2015JC011174

Freund, M. B., Henley, B. J., Karoly, D. J., McGregor, H. V., Abram, N. J., & Dommenget, D. (2019). Higher frequency of Central Pacific El Niño events in recent decades relative to past centuries. *Nature Geoscience*, *12*(6), 450–455.

Ghanbari, M., Arabi, M., Obeysekera, J., & Sweet, W. (2019). A coherent statistical model for coastal flood frequency analysis under nonstationary sea level conditions. *Earth's Future*, *7*(2), 162–177.

Haigh, I. D., MacPherson, L. R., Mason, M. S., Wijeratne, E. M. S., Pattiaratchi, C. B., Crompton, R. P., & George, S. (2014). Estimating present day extreme water level exceedance probabilities around the coastline of Australia: Tropical cyclone-induced storm surges. *Climate Dynamics*, *42*(1–2), 139–157.

Haigh, I. D., Nicholls, R., & Wells, N. (2010). A comparison of the main methods for estimating probabilities of extreme still water levels. *Coastal Engineering*, *57*(9), 838–849.

Haigh, I. D., Pickering, M. D., Green, J. M., Arbic, B. K., Arns, A., Dangendorf, S., et al. (2020). The tides they are a-Changin': A comprehensive review of past and future nonastronomical changes in tides, their driving mechanisms, and future implications. *Reviews of Geophysics*, *58*(1), e2018RG000636. https://doi.org/10.1029/2018RG000636

Hermans, T. H., Le Bars, D., Katsman, C. A., Camargo, C. M., Gerkema, T., Calafat, F. M., et al. (2020). Drivers of interannual sea level variability on the northwestern European shelf. *Journal of Geophysical Research: Oceans*, *125*(10), e2020JC016325. https://doi.org/10.1029/2020JC016325

Hinkel, J., Feyen, L., Hemer, M., Le Cozannet, G., Lincke, D., Marcos, M., et al. (2021). Uncertainty and bias in global to regional scale assessments of current and future coastal flood risk. *Earth's Future*, *9*(7), e2020EF001882. https://doi.org/10.1029/2020EF001882

Hovmöller, E. (1949). The trough-and-ridge diagram. *Tellus*, *1*, 62–66. https://doi.org/10.3402/tellusa.v1i2.8498

Huang, B., Banzon, V. F., Freeman, E., Lawrimore, J., Liu, W., Peterson, T. C., et al. (2015). *Extended Reconstructed Sea Surface Temperature (ERSST), version 4*. NOAA National Centers for Environmental Information. [08/2018]. https://doi.org/10.7289/V5KD1VVF

Krapp, M., Beyer, R. M., Edmundson, S. L., Valdes, P. J., & Manica, A. (2021). A statistics-based reconstruction of high-resolution global terrestrial climate for the last 800,000 yr. *Scientific Data*, *8*(1), 1–18.

Kriebel, D. L., Geiman, J. D., & Henderson, G. R. (2015). Future flood frequency under sea-level rise scenarios. *Journal of Coastal Research*, *31*(5), 1078–1083.

Kwon, H. H., Lall, U., & Khalil, A. F. (2007). Stochastic simulation model for nonstationary time series using an autoregressive wavelet decomposition: Applications to rainfall and temperature. *Water Resources Research*, *43*(5). https://doi.org/10.1029/2006WR005258

Lafleur, D. M., Barrett, B. S., & Henderson, G. R. (2015). Some climatological aspects of the Madden–Julian Oscillation (MJO). *Journal of Climate*, *28*(15), 6039–6053.

Lang, A., & Mikolajewicz, U. (2019). The long-term variability of extreme sea levels in the German Bight. *Ocean Scienc*e, *15*, 651–668. https://doi.org/10.5194/os-15-651-2019

Leonard, M., Westra, S., Phatak, A., Lambert, M., van den Hurk, B., McInnes, K., et al. (2014). A compound event framework for understanding extreme impacts. *Wiley Interdisciplinary Reviews: Climate Change*, *5*(1), 113–128.

Leung, M., Ruggiero, P., Anderson, D., Mendez, F. J., Rueda, A., & Bolte, J. (2019). Incorporating a probabilistic climate emulator into an agent-based coastal futures forecasting system. In *Coastal sediments 2019: Proceedings of the 9th International Conference* (pp. 1152–1159).

Li, J., Xie, S. P., Cook, E. R., Morales, M. S., Christie, D. A., Johnson, N. C., et al. (2013). El Niño modulations over the past seven centuries. *Nature Climate Change*, *3*(9), 822–826.

Marcos, M., Calafat, F. M., Berihuete, Á., & Dangendorf, S. (2015). Long-term variations in global sea level extremes. *Journal of Geophysical Research: Oceans*, *120*, 8115–8134. https://doi.org/10.1002/2015JC011173

Marra, J. J., Sweet, W. V., Leuliette, E., Kruk, M., Genz, A. S., Storlazzi, C. D., et al. (2022). Advancing best practices for the analysis of the vulnerability of military installations in the Pacific basin to coastal flooding under a changing climate—RC-2644: Final Report for the U.S. Department of Defense Strategic Environmental Research and Development Program (p. 543). 1 June 2022.

McCabe, G. J., Betancourt, J. L., Gray, S. T., Palecki, M. A., & Hidalgo, H. G. (2008). Associations of multi-decadal sea-surface temperature variability with U.S. drought. *Quaternary International*, *188*(1), 31–40.

Menéndez, M., & Woodworth, P. L. (2010). Changes in extreme high water levels based on a quasi-global tide-gauge data set. *Journal of Geophysical Research: Oceans*, *115*(C10). https://doi.org/10.1029/2009JC005997

Mentaschi, L., Vousdoukas, M., Voukouvalas, E., Sartini, L., Feyen, L., Besio, G., & Alfieri, L. (2016). The transformed-stationary approach: A generic and simplified methodology for non-stationary extreme value analysis. *Hydrology and Earth System Sciences*, *20*(9), 3527–3547.

Merrifield, M. A., Thompson, P. R., & Lander, M. (2012). Multidecadal sea level anomalies and trends in the western tropical Pacific. *Geophysical Research Letters*, *39*(13). https://doi.org/10.1029/2012GL052032

Moftakhari, H. R., AghaKouchak, A., Sanders, B. F., Feldman, D. L., Sweet, W., Matthew, R. A., & Luke, A. (2015). Increased nuisance flooding along the coasts of the United States due to sea level rise: Past and future. *Geophysical Research Letters*, *42*, 9846–9852. https://doi.org/10.1002/2015GL066072

Moftakhari, H. R., AghaKouchak, A., Sanders, B. F., & Matthew, R. A. (2017). Cumulative hazard: The case of nuisance flooding. *Earth's Future*, *5*, 214–223. https://doi.org/10.1002/2016EF000494

Muis, S., Verlaan, M., Winsemius, H. C., Aerts, J. C., & Ward, P. J. (2016). A global reanalysis of storm surges and extreme sea levels. *Nature Communications*, *7*(1), 1–12.

Mukhopadhyay, S., Leung, M., Cagigal, L., Kucharski, J., Ruggiero, P., & Steinschneider, S. (2022). A paleo-proxy-based reconstruction of still water level in the San Francisco Bay during 1500–2000 CE (Version v0) [Dataset]. Zenodo. https://doi.org/10.5281/zenodo.7455978

Mukhopadhyay, S., Patskoski, J. M., & Sankarasubramanian, A. (2018). Role of Pacific SSTs in improving reconstructed streamflow over the coterminous U.S. *Scientific Reports*, *8*(1), 1–9.

Nederhoff, K., Saleh, R., Tehranirad, B., Herdman, L., Erikson, L., Barnard, P. L., & Van der Wegen, M. (2021). Drivers of extreme water levels in a large, urban, high-energy coastal estuary—A case study of the San Francisco Bay. *Coastal Engineering*, *170*, 103984.

Nelsen, R. B. (2007). *An introduction to copulas*. Springer Science & Business Media.

Neukom, R., Nash, D. J., Endfield, G. H., Grab, S. W., Grove, C. A., Kelso, C., et al. (2014). Multi-proxy summer and winter precipitation reconstruction for southern Africa over the last 200 yr. *Climate Dynamics*, *42*(9), 2713–2726.

Neumann, B., Vafeidis, A. T., Zimmermann, J., & Nicholls, R. J. (2015). Future coastal population growth and exposure to sea-level rise and coastal flooding-a global assessment. *PLoS One*, *10*(3), e0118571.

Nurhati, I. S., Cobb, K. M., & Di Lorenzo, E. (2011). Decadal-scale SST and salinity variations in the central tropical Pacific: Signatures of natural and anthropogenic climate change. *Journal of Climate*, *24*(13), 3294–3308.

Orton, P. M., Hall, T. M., Talke, S. A., Blumberg, A. F., Georgas, N., & Vinogradov, S. (2016). A validated tropical-extratropical flood hazard assessment for New York Harbor. *Journal of Geophysical Research: Oceans*, *121*(12), 8904–8929. https://doi.org/10.1002/2016JC011679

Osman, M. B., Tierney, J. E., Zhu, J., Tardif, R., Hakim, G. J., King, J., & Poulsen, C. J. (2021). Globally resolved surface temperatures since the last glacial maximum. *Nature*, *599*(7884), 239–244.

Parker, K., Ruggiero, P., Serafin, K. A., & Hill, D. F. (2019). Emulation as an approach for rapid estuarine modeling. *Coastal Engineering*, *150*, 79–93.

Peng, D., Hill, E. M., Meltzner, A. J., & Switzer, A. D. (2019). Tide gauge records show that the 18.61 yr nodal tidal cycle can change high water levels by up to 30 cm. *Journal of Geophysical Research: Oceans*, *124*, 736–749. https://doi.org/10.1029/2018JC014695

Perez, J., Méndez, F. J., Menéndez, M., & Losada, I. J. (2014). ESTELA: A method for evaluating the source and travel time of the wave energy reaching a local area. *Ocean Dynamics*, *64*(8), 1181–1191. https://doi.org/10.1007/s10236-014-0740-7

Rashid, M. M., Wahl, T., & Chambers, D. P. (2021). Extreme sea level variability dominates coastal flood risk changes at decadal time scales. *Environmental Research Letters*, *16*, 024026.

Rashid, M. M., Wahl, T., Chambers, D. P., Calafat, F. M., & Sweet, W. V. (2019). An extreme sea level indicator for the contiguous United States coastline. *Scientific Data*, *6*, 326. https://doi.org/10.1038/s41597-019-0333-x

Ray, R. D., & Foster, G. (2016). Future nuisance flooding at Boston caused by astronomical tides alone. *Earth's Future*, 4, 578–587. https://doi.org/10.1002/2016EF000423

Razavi, S., Elshorbagy, A., Wheater, H., & Sauchyn, D. (2016). Time scale effect and uncertainty in reconstruction of paleo-hydrology. *Hydrological Processes*, *30*(13), 1985–1999.

R Core Team. (2021). *R: A language and environment for statistical computing*. R Foundation for Statistical Computing. Retrieved from https://www.R-project.org/

Rueda, A., Camus, P., Tomás, A., Vitousek, S., & Méndez, F. J. (2016). A multivariate extreme wave and storm surge climate emulator based on weather patterns. *Ocean Modeling*, *104*, 242–251.

Saha, S., Moorthi, S., Wu, X., Wang, J., Nadiga, S., Tripp, P., et al. (2011). *NCEP Climate Forecast System Version 2 (CFSv2) selected hourly time-series products*. Research data archive at the National Center for Atmospheric Research, Computational and Information Systems Laboratory. https://doi.org/10.5065/D6N877VB

Sanchez, S. C., Westphal, N., Haug, G. H., Cheng, H., Edwards, R. L., Schneider, T., et al. (2020). A continuous record of central tropical Pacific climate since the mid-nineteenth century reconstructed from Fanning and Palmyra Island corals: A case study in coral data reanalysis. *Paleoceanography and Paleoclimatology*, *35*(8), e2020PA003848. https://doi.org/10.1029/2020PA003848

Serafin, K. A., & Ruggiero, P. (2014). Simulating extreme total water levels using a time-dependent, extreme value approach. *Journal of Geophysical Research: Oceans*, *119*(9), 6305–6329. https://doi.org/10.1002/2014JC010093

Serafin, K. A., Ruggiero, P., & Stockdon, H. F. (2017). The relative contribution of waves, tides, and nontidal residuals to extreme total water levels on U.S. West Coast sandy beaches. *Geophysical Research Letters*, *44*(4), 1839–1847. https://doi.org/10.1002/2016GL071020

Steinschneider, S., Ho, M., Cook, E. R., & Lall, U. (2016). Can PDSI inform extreme precipitation?: An exploration with a 500 yr long paleoclimate reconstruction over the U.S. *Water Resources Research*, *52*(5), 3866–3880. https://doi.org/10.1002/2016WR018712

Steinschneider, S., Ho, M., Williams, A. P., Cook, E. R., & Lall, U. (2018). A 500 yr tree-ring based reconstruction of extreme cold-season precipitation and number of atmospheric river landfalls across the Southwestern U.S. *Geophysical Research Letters*, *45*, 5672–5680. https://doi.org/10.1029/2018GL078089

Sweet, W. V., Dusek, G., Obeysekera, J., & Marra, J. J. (2018). *Patterns and projections of high tide flooding along the U.S. coastline using a common impact threshold*. NOAA Technical Report NOS CO-OPS 086. February, Retrieved from https://repository.library.noaa.gov/view/noaa/17403

Sweet, W. V., Hamlington, B. D., Kopp, R. E., Weaver, C. P., Barnard, P. L., Bekaert, D., et al. (2022). *Global and regional sea level rise scenarios for the United States: Updated mean projections and extreme water level probabilities along U.S. Coastlines (NOAA Technical report NOS 01)* (p. 111). National Oceanic and Atmospheric Administration, National Ocean Service, Silver Spring, MD. https://oceanservice.noaa.gov/hazards/sealevelrise/noaa-nos-techrpt01-global-regional-SLR-scenarios-US.pdf

Sweet, W. V., & Park, J. (2014). From the extreme to the mean: Acceleration and tipping points of coastal inundation from sea level rise. *Earth's Future*, *2*, 579–600. https://doi.org/10.1002/2014EF000272

Taherkhani, M., Vitousek, S., Barnard, P. L., Frazer, N., Anderson, T. R., & Fletcher, C. H. (2020). Sea-level rise exponentially increases coastal flood frequency. *Scientific Reports*, *10*, 6466. https://doi.org/10.1038/s41598-020-62188-4

Thompson, P. R., & Mitchum, G. T. (2014). Coherent sea level variability on the North Atlantic western boundary. *Journal of Geophysical Research: Oceans*, *119*(9), 5676–5689. https://doi.org/10.1002/2014JC009999

Thompson, P. R., Widlansky, M. J., Hamlington, B. D., Merrifield, M. A., Marra, J. J., Mitchum, G. T., & Sweet, W. (2021). Rapid increases and extreme months in projections of United States high-tide flooding. *Nature Climate Change*, *11*, 584–590. https://doi.org/10.1038/s41558-021-01077-8

Tierney, J. E., Abram, N. J., Anchukaitis, K. J., Evans, M. N., Giry, C., Kilbourne, K. H., et al. (2015). Tropical sea surface temperatures for the past four centuries reconstructed from coral archives. *Paleoceanography*, *30*(3), 226–252.

Trenberth, K., Fasullo, J., & Shepherd, T. (2015). Attribution of climate extreme events. *Nature Climate Change*, *5*, 725–730. https://doi.org/10.1038/nclimate2657

Vitousek, S., Barnard, P. L., Fletcher, C. H., Frazer, N., Erikson, L., & Storlazzi, C. D. (2017). Doubling of coastal flooding frequency within decades due to sea-level rise. *Scientific Reports*, *7*(1), 1–9.

Wahl, T., & Chambers, D. P. (2015). Evidence for multidecadal variability in U.S. extreme sea level records. *Journal of Geophysical Research: Oceans*, *120*(3), 1527–1544. https://doi.org/10.1002/2014JC010443

Wahl, T., & Chambers, D. P. (2016). Climate controls multidecadal variability in U.S. extreme sea level records. *Journal of Geophysical Research: Oceans*, *121*(2), 1274–1290. https://doi.org/10.1002/2015JC011057

Wahl, T., Haigh, I. D., Nicholls, R. J., Arns, A., Dangendorf, S., Hinkel, J., & Slangen, A. B. (2017). Understanding extreme sea levels for broad-scale coastal impact and adaptation analysis. *Nature Communications*, *8*(1), 1–12.

Wheeler, M. C., & Hendon, H. H. (2004). An all-season real-time multivariate MJO index: Development of an index for monitoring and prediction. *Monthly Weather Review*, *132*, 1917–1932. https://doi.org/10.1175/1520-0493(2004)132<1917:AARMMI>2.0.CO;2

Williams, A. P., Anchukaitis, K. J., Woodhouse, C. A., Meko, D. M., Cook, B. I., Bolles, K., & Coon, E. R. (2021). Tree rings and observations suggest no stable cycles in Sierra Nevada cool-season precipitation. *Water Resources Research*, *57*(3), e2020WR028599. https://doi.org/10.1029/2020WR028599

Wilson, R., Cook, E., D'Arrigo, R., Riedwyl, N., Evans, M. N., Tudhope, A., & Allan, R. (2010). Reconstructing ENSO: The influence of method, proxy data, climate forcing, and teleconnections. *Journal of Quaternary Science*, *25*(1), 62–78.

Woodhouse, C. A., Meko, D. M., MacDonald, G. M., Stahle, D. W., & Cook, E. R. (2010). A 1,200 yr perspective of 21st century drought in southwestern North America. *Proceedings of the National Academy of Sciences*, *107*(50), 21283–21288.

Zhang, L., & Singh, V. (2019). Copulas and their properties. In *Copulas and their applications in water resources engineering* (pp. 62–122). Cambridge University Press. https://doi.org/10.1017/9781108565103.004

Zheng, Z., Jin, L., Li, J., Chen, J., Zhang, X., & Wang, Z. (2021). Moisture variation inferred from tree rings in north central China and its links with the remote oceans. *Scientific Reports*, *11*(1), 1–14.

Erratum

In the originally published version of this article, the text in the caption for Figure 7 contained some errors. "1990" has been corrected to "1900" and "97. Fifth" has been corrected to "97.5th." In addition, the caption for Figure 8 contains an error. "1990" has been corrected to "1900." This may be considered the authoritative version of record.